Intrusive history and petrogenesis of the Ash Mountain Complex, Sierra Nevada batholith, California (USA)

Julia E. Holland[1,*], Benjamin Surpless[1], Diane R. Smith[1,†], Staci L. Loewy[2], and Jade Star Lackey[3]
[1]*Department of Geosciences, Trinity University, One Trinity Place, San Antonio, Texas 78212-7200, USA*
[2]*Department of Geological Sciences, University of Texas at Austin, 1 University Station C1100, Austin, Texas 78712, USA*
[3]*Department of Geology, Pomona College, 185 E. Sixth Street, Claremont, California 91711, USA*

ABSTRACT

The Ash Mountain Complex (AMC) in the western Sierra Nevada batholith (SNB; California, USA) is an exposure of six compositionally diverse intrusive lithologies with clear crosscutting relationships that permit a focused investigation of magma source characteristics and the relative roles of petrogenetic processes on the evolution of the system. We use new field observations, zircon U-Pb dates, major and trace element data, and Sr-Nd-Pb isotopic data to develop a model that can be applied to similar SNB intrusive suites. Stage 1 units, emplaced ca. 105 Ma, consist of two gabbros, a gabbrodiorite, and a granite. Stage 2 and stage 3 units were emplaced ca. 104 Ma and ca. 103 Ma, respectively, and are granites. We suggest that stage 1 gabbroids were derived by partial melting of lithospheric mantle, whereas coeval felsic magmas were derived by partial melting of a mafic, juvenile crustal source. Stage 2 and stage 3 granitoids were derived from similar sources that generated stage 1 granitoids, but there was greater input from evolved crust. Fractionation and/or assimilation played only a minor role in system evolution. Past studies of SNB magmas have come to conflicting conclusions about the petrogenesis of intermediate magmas that dominate the batholith; we hypothesize that mafic and felsic end members of the AMC could represent end members in mixing processes that generate these magmas. The timing of emplacement of the AMC coincides with a transition of magmatic style in the SNB, from smaller volume magmatic suites with mixed mantle and crustal sources to larger volume magmatic suites derived from greater proportions of crust.

*Present address: Department of Geological Sciences, The University of Texas at Austin, 1 University Station C1100, Austin, Texas 78712, USA
†Corresponding author email: dsmith@trinity.edu

INTRODUCTION

The interplay of source melting dynamics, fractional crystallization, and magma hybridization by mixing and assimilation generates a wide variety of granitic magmas. Granitoid rocks of calc-alkaline batholiths, forming at the fringes of continents, are particularly intriguing as they can chemically record the variable reworking of preexisting crust, accreted island arc terranes, mafic underplate, and/or lithospheric mantle. Although the net contribution to crustal growth by continental arc magmatism remains uncertain, there is growing evidence that continental arc processes act to transform accreted terranes into bona fide continental crust (e.g., Lee et al., 2007; Lackey et al., 2012). Discoveries that texturally homogeneous granodiorite plutons may be incrementally constructed over time scales of several million years (e.g., Coleman et al., 2004; Davis et al., 2012) highlight the need for better understanding of magma sources and mixing processes in the upper mantle and lower crust of magmatic arcs. With that goal in mind, we targeted the intrusive Ash Mountain Complex (AMC) in the foothills of Sequoia National Park (California, USA). Previously documented Sr isotopic data for samples from areas near the AMC (Chen and Tilton, 1991) show that the initial $^{87}Sr/^{86}Sr$ (Sr_i) = 0.706 line, which roughly denotes the boundary between accreted terranes underlying the western Sierra Nevada batholith (SNB) and continental crust underlying the eastern SNB, is immediately west of the AMC (Fig. 1). Therefore, a range of source and contamination scenarios is possible for the petrogenesis of magmas emplaced in the region.

While workers suggest that fractional crystallization could account for the large compositional diversity exhibited within the SNB (e.g., Bowen, 1928; Bateman and Chappell, 1979), others (e.g., Reid et al., 1993; Sisson et al., 1996) found that chemical data for the SNB are largely inconsistent with that hypothesis. Other workers proposed that mixing and mingling of mafic and silicic end-member magmas were important in generating this diversity (e.g., Reid et al., 1983; Frost and Mahood, 1987; Dorais et al., 1990; Sisson et al., 1996; Ratajeski et al., 2001; Wenner and Coleman, 2004; Pignotta et al., 2010).

Although mixing of high- and low-SiO_2 magmas may contribute to the majority of granodiorite crust, the origin of the felsic end member involved with mixing is not entirely understood and may involve more than one source (Wenner and Coleman, 2004). For example, partial melting of intermediate country rock may generate high-SiO_2 melts (e.g., Skjerlie and Johnston, 1993; Patiño-Douce, 1997), but mafic underplate and hydrous cumulates may also partially melt to generate high-SiO_2 magmas (e.g., Rushmer, 1991; Ratajeski et al., 2005; Sisson et al., 2005). Growing evidence suggests that heat flux provided by magmatic recharge (e.g., Bergantz, 1989; Dufek and Bergantz, 2005; Annen et al., 2006) is sufficient to drive voluminous melting of fertile crustal sources. Such crustal rocks may be drawn down by return flow along the margins of growing plutons, and potentially be inserted into magma source regions (Saleeby et al., 2003) or underthrust into these source regions by forearc or retroarc compressional deformation (Ducea, 2001; Ducea and Barton, 2007; DeCelles et al., 2009).

In this study we investigate the ca. 105 Ma (Holland et al., 2010) comagmatic gabbro to granite AMC in the Kaweah River valley to evaluate felsic magma source characteristics as well as processes of magma differentiation. We use major and trace element and isotope geochemistry of these rocks to evaluate the relative roles of partial melting, mixing, mingling, and assimilation–fractional crystallization (AFC) in the origin of AMC magmas. In addition, we interpret single zircon isotopic and trace element data to determine absolute ages and to evaluate petrogenetic processes. Memeti et al. (2010a) and

Geosphere; August 2013; v. 9; no. 4; p. 691–717; doi:10.1130/GES00890.1; 22 figures; 7 tables; 2 supplemental files.
Received 11 December 2012 ♦ Revision received 7 May 2013 ♦ Accepted 18 June 2013 ♦ Published online 16 July 2013

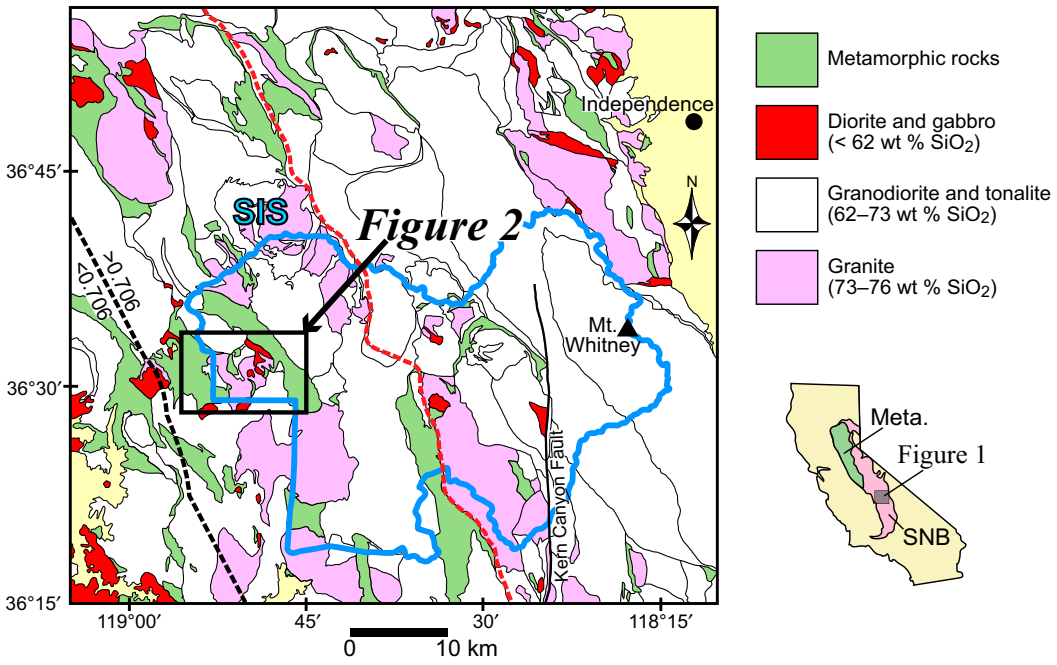

Figure 1. Geologic map of the south-central Sierra Nevada batholith (SNB; after Moore, 2001). Lower right inset shows map location in California. SIS denotes the location of the Sequoia Intrusive Suite. The black dashed line represents the regional 0.706 $(^{87}Sr/^{86}Sr)_i$ isopleth (Kistler and Peterman, 1973, 1978; DePaolo, 1980, 1981; Kistler et al., 1986; Chen and Tilton, 1991). The red dashed line separates the western and eastern SNB based on Sr and O isotopes as well as relationships of rock types in roof pendants (Kistler, 1990). The blue line is the boundary of Sequoia National Park. The black box indicates the map area shown in Figure 2.

Davis et al. (2012) used detailed analyses of single zircon crystals to evaluate the emplacement history of large-volume, intermediate intrusive suites of the eastern Sierra Nevada, but a similar method has not been applied to compositionally diverse, mingled or mixed magmas in the SNB. In cases where this type of analysis has been applied to mixed magmatic systems like the zoned Spirit Mountain batholith in Nevada (Claiborne et al., 2010), it has proven especially powerful for evaluating the relative importance of magma mixing and crystallization processes.

Emplacement timing of the AMC is also significant within the context of SNB Cretaceous magmatism. The ca. 108–105 Ma period has been recognized (Lackey et al., 2012) as an important period of transition of magmatic style in the Sierra Nevada, from smaller volume magmatic suites dominated by mixed mantle and crustal sources and recycling of accreted terranes to larger volume magmatic suites derived from greater proportions of remelted, preexisting arc crust including local crust or underthrust rocks. Therefore, the AMC may provide critical insights into the nature of coeval and proximal mafic and felsic magmas during this period.

GEOLOGIC SETTING

The SNB formed during the prolonged eastward subduction of the Farallon plate below the North American continent (e.g., Dickinson, 1981). The system was active for more than 140 m.y., from the Triassic to the Late Cretaceous (e.g., Stern et al., 1981; Chen and Moore, 1982), but most magmatic activity occurred in two brief episodes. The first pulse of volumetrically significant magmatism lasted from ca. 180 to 165 Ma in the Jurassic, with a significantly more voluminous phase between 102 and 85 Ma (e.g., Coleman and Glazner, 1997; Ducea, 2001; Wenner and Coleman, 2004; Coleman et al., 2004; Memeti et al., 2010a; Davis et al., 2012).

The majority of exposed rocks in the SNB are intermediate (granodiorite) in composition (e.g., Bateman, 1992; Fig. 1), but the common occurrence of these rocks with coeval low- and high-silica rocks (e.g., Coleman et al., 1995; Ratajeski et al., 2001; Wenner and Coleman, 2004) suggests a possible common genetic origin (Frost and Mahood, 1987). Accumulation of a thick lithospheric root beneath the Sierran arc is deduced to have occurred in at least the Late Cretaceous, as recorded by pressure-temperature-time conditions and isotopic ratios of garnet pyroxenite and garnet-hornblende granulite xenoliths in the central SNB (Dodge et al., 1986, 1988; Mukhopadhyay and Manton, 1994; Lee et al., 2000, 2006; Ducea, 2001, 2002). Ducea (2002) used elemental compositions and isotopic ratios for these xenoliths to argue that SNB granitoids and the xenoliths are the melts and residues, respectively, resulting from partial melting at depths exceeding ~35–40 km.

In the region surrounding the AMC, Cretaceous intrusive rocks, dominantly quartz diorite to granodiorite, with minor gabbro and diorite, range in age from 133 to 97 Ma (Sisson and Moore, 1994; Fig. 2). The Frys Point granite and the Milk Ranch Peak granodiorite are the largest local plutons, while quartz diorite, diorite, and gabbro are most commonly found as isolated bodies within the Frys Point granite (Fig. 2). Metamorphic pendants are found near several sample localities (Fig. 2).

Prior studies of these adjacent intrusive rocks were largely restricted to regional mineralogical, trace element (Ague and Brimhall, 1988), and Sr, Pb, Nd, and O isotopic studies (DePaolo, 1981; Kistler, 1990; Chen and Tilton, 1991; Wenner and Coleman, 2004; Lackey et al., 2006, 2008). These investigations included rocks proximal to (and possibly part of) the AMC, including the Frys Point granite and some gabbro bodies. Magmas in the region interacted with abundant Triassic to Cretaceous (Chen and Moore, 1982; Sisson and Moore, 1994) pendants and septa of carbonaceous metamorphic wall-rocks (Figs. 1 and 2), based on mineralogical and mineral chemistry redox indicators (Ague and Brimhall, 1988; Lackey et al., 2006). Isotopic studies provide further evidence for localized contamination (Chen and Tilton, 1991; Lackey et al., 2006, 2008) and suggest that both mafic and felsic rocks were derived from sources with crustal affinities (e.g., high $\delta^{18}O$, high Sr_i, high Pb_i; Wenner and Coleman, 2004; Lackey et al., 2006). For example, $\delta^{18}O$ (zircon) values for the low-SiO_2 (~47 wt%) Elk Creek Gabbro body in the AMC (unit KJgb, Fig. 2) are ~8.3‰ (Lackey et al.,

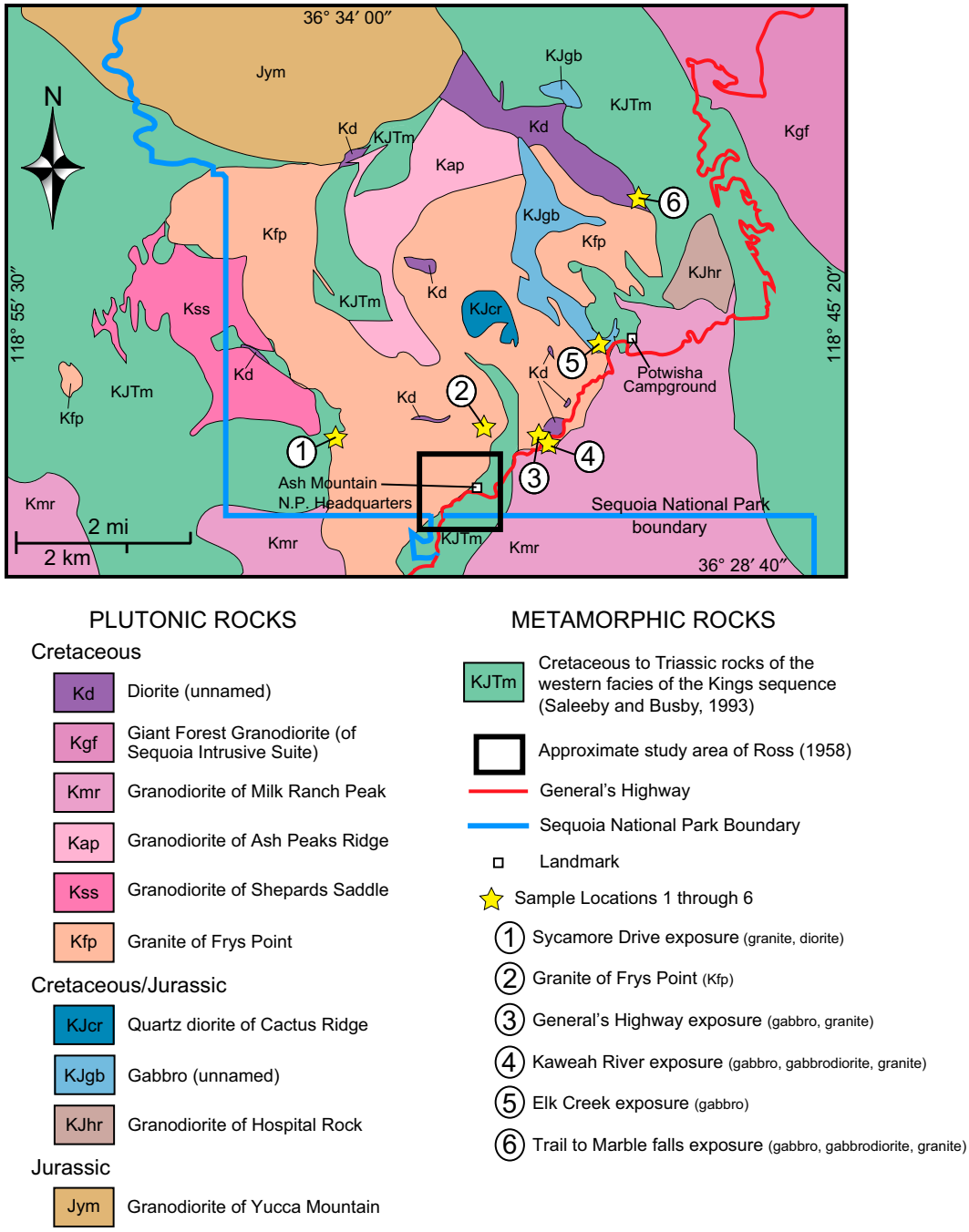

Figure 2. Geologic map of the Ash Mountain Complex and surrounding region, modified from Sisson and Moore (1994) and Moore (2001). The black box denotes the approximate location of the Ash Mountain Complex as defined by Ross (1958). See Figure 1 for map location. See Table 2 for petrographic and geochemical data for samples taken from locations 1 through 6.

2006), higher than many granites in the SNB (Lackey et al., 2008) and suggestive of melting of crustal sources.

Ash Mountain Complex

Ross (1958, p. 6) initially described the AMC in southwestern Sequoia National Park (Figs. 1 and 2) with field observations limited to an area of ~2.6 km^2 "in the vicinity of the Ash Mountain Park headquarters"; he identified four intrusive lithologies, including a quartz diorite, a granite, a gray, fine-grained intrusive (unclassified), and a dark fine-grained intrusive (unclassified). Ross (1958) was not able to determine a clear chronology of intrusion, in large part due to mutually crosscutting relations, with observations from different localities suggesting conflicting chronologies of intrusion. We expand the area of the AMC to include exposures along the Kaweah River, based on the similar diversity in intrusive compositions and the relative proximity of the Kaweah River exposure to the AMC as defined by Ross (1958).

METHODS

Sample Collection and Preparation

We sampled each of the six AMC units identified in fresh outcrop exposures along the Kaweah River (location 4 in Fig. 2) for petrographic and geochemical analyses. We also collected samples representing the compositional range of AMC intrusive lithologies from other localities (locations 1, 2, 3, 5, and 6 in Fig. 2) in order to provide a broader regional context for the AMC sampling.

We prepared whole-rock powders for geochemical analysis by standard chipping and pulverizing (2 min) in a Rocklabs tungsten carbide head and swing mill, which was cleaned with quartz sand between samples. We used standard hydraulic, gravimetric, and magnetic separation techniques to concentrate zircon grains, employing a Rogers concentrating table, methylene iodide (density 3.32 g/cm^3), and a Frantz magnetic separator. We performed final zircon purification by hand-picking under a petrographic microscope.

X-Ray Fluorescence Major and Trace Element Geochemistry

We measured major and selected trace elements for 19 samples by X-ray fluorescence (XRF) (Table 1) at Pomona College. We vortex blended rock powder and flux in a 1:2 ratio (3.5 g powder to 7.0 g dilithium tetraborate), and fused these mixtures to glass beads in graphite crucibles heated at 1000 °C for 10 min. We reground the beads and fused them a second time, polished the beads on diamond laps, and analyzed the polished beads. We determined concentrations according to calibrations based on 55 certified reference materials that span a large range of compositions (see Lackey et al., 2012, for further details regarding XRF analysis at Pomona College). Typical analytical 2 standard deviation uncertainties for analyses (in wt%) of major elements, determined conservatively as reproducibility of multiple beads produced from a sample or standard powder, are ±0.15% (SiO_2); 0.06%–0.07% (Fe_2O_3, Al_2O_3); 0.02%–0.05% (Na_2O, K_2O, MgO, CaO); <0.004% (TiO_2, MnO, P_2O_5). Trace element uncertainties (±2 standard deviations) are 1 ppm (La, Pr, Hf), 2 ppm (Nd, Cu, Ga, Nb, Pb, Rb, Th, U, Y, Zr) to 3 ppm (Cr, Sc, Sr, V); other elements have higher uncertainties: Ce (4 ppm), Zn (6 ppm), Ni (7 ppm), Ba (30 ppm).

Zircon Sensitive High-Resolution Ion Microprobe–Reverse Geometry U-Pb Dating and Trace Element Geochemistry

We used methods described by Barth and Wooden (2010) to analyze U-Pb isotopes in zircon grains from the AMC. Based on relative ages deduced from field relationships (see discussion of Field Relationships in following), we selected four samples from Kaweah River units Kgp, Kgd, Kgr, and Kp for sensitive high-resolution ion microprobe (SHRIMP) U-Pb dating to constrain the emplacement timing of intrusions of stages 1, 2, and 3. We also selected a sample from the Frys Point intrusion (AMC unit Kfp; 10SQ21) for SHRIMP U-Pb dating. We selected the most inclusion-free zircon grains for age and geochemical analysis and mounted those zircon grains on double-sided tape, which we then cast in epoxy and cured overnight. We ground and polished the mount to a 1 µm finish to expose zircon interiors. We then imaged the zircon grains using reflected light on a petrographic microscope and on a scanning electron microscope using a Hamamatsu photo multiplier tube for cathodoluminescence (CL) imaging. We washed the mounts, rinsed them with deionized water, dried them, and coated them in gold to ensure a conductive surface on the mount.

Using the reflected light and CL images, we screened zircon grains to avoid areas with high Th/U loss, melt inclusions, and/or inherited cores. We used a primary oxygen beam (O_2^-), varying in intensity from 5 to 10 nA, to sputter 20–40-µm-diameter spots to a depth of 1–2 µm within zircon grains (Barth and Wooden, 2010). We used sputtering times of 9–12 min per spot to generate secondary ion beam fluxes (Barth and Wooden, 2010). We recorded isotopes beginning with a high mass normalizing species ($^{90}Zr_2^{16}O^+$) followed by an array of other isotopes, specifically $^{204}Pb^+$, $^{206}Pb^+$, $^{207}Pb^+$, $^{208}Pb^+$, $^{238}U^+$, $^{232}Th^{16}O^+$, $^{238}U^{16}O^+$, $^{232}Th^+$, ^{232}Th, and $^{270}UO_2$, using ratios of $^{206}Pb/^{238}U$ to calculate ages (Barth and Wooden, 2010). We measured a set of 9–10 rare earth elements (REEs), Y and Hf (1 s/mass) at mass (M) resolutions of M/DM = 7500–8500 (DM is the width of a peak measured at mass M), which is sufficient to eliminate interfering molecular species (Barth and Wooden, 2010). We used the Hf analyses to constrain crystallization temperatures and cooling rates (Barth and Wooden, 2010).

We standardized zircon grains selected for geochronology against R33 Braintree Complex zircon (419 Ma; Black et al., 2004), and we standardized zircon grains selected for U, Th, and trace element analysis against Madagascar Green (MAD) zircon (Mazdab and Wooden, 2006). Samples were bracketed at an average interval of one standard for every four unknown samples (Barth and Wooden, 2010). We completed data reduction geochronology using MS Excel Macros Squid (Barth and Wooden, 2010) and Isoplot (Ludwig, 2000), based on the methods of Williams (1997) and Ireland and Williams (2003). Interpreted zircon ages exclude grains that are significantly discordant or are distinctly older (antecrysts and xenocrysts) or younger (Pb loss) than the majority of the population. In most cases, only one or two grains were excluded from interpreted ages (see Supplemental Table 1[1]).

[1]Supplemental Table 1. U-Pb and other geochemical data for zircons. If you are viewing the PDF of this paper or reading it offline, please visit http://dx.doi.org/10.1130/GES00890.S1 or the full-text article on www.gsapubs.org to view Supplemental Table 1.

Isotope Geochemistry

We analyzed samples for isotope geochemistry at the University of Texas at Austin. We leached whole-rock powders in 2.5N HCl at 60 °C for 20 min and dissolved these powders in Teflon bombs using 29N HF and 16N HNO_3 for 5 days in a 190 °C oven, followed 6N HCl for 1 day in a 180 °C oven. We separated Pb, Sr, Nd, and Sm from the same aliquot using column chromatography, AG 1x-8 resin with HCl for Pb, Sr spec resin for Sr, and Re-Spec and HDEHP for Nd and Sm. We analyzed all samples on Re filaments using a Triton thermal ionization mass spectrometer. We loaded Pb with silica gel and Sr with Ta_2O_5 onto single filaments. We analyzed Sm and Nd as a metal, using double filaments. We corrected Sr, Nd, and Sm ratios for exponential fractionation using $^{88}Sr/^{86}Sr = 8.375209$ and $^{146}Nd/^{144}Nd = 0.7219$ and $^{152}Sm/^{147}Sm = 1.783078$. We corrected Pb ratios for fractionation using the ^{208}Pb-^{204}Pb double spike method and the calculation of Hamelin et al. (1985). We corrected ^{87}Sr for ^{87}Rb by simultaneous measurement of ^{85}Rb and $^{87}Rb/^{85}Rb = 0.38600$ and corrected ^{144}Nd for ^{144}Sm by simultaneous measurement of ^{147}Sm and $^{147}Sm/^{144}Sm = 0.206700$. The mean ratios for standards analyzed over 6 mo during the time of analyses are $^{87}Sr/^{86}Sr = 0.710271 \pm 9$ (2 standard deviation, n = 39) for NBS 987, $^{143}Nd/^{144}Nd = 0.512069 \pm 8$ (2 standard deviations, n = 8) for Ames Nd, and $^{206}Pb/^{204}Pb = 16.934 \pm 6$, $^{207}Pb/^{204}Pb = 15.488 \pm 3$, and $^{208}Pb/^{204}Pb = 36.687 \pm 4$ (2 standard deviations, n = 2) for NBS 981 by the double spike method. Measured full procedural blanks were small and insignificant relative to the amount of Sr, Nd, Sm, and Pb in samples.

RESULTS

Field Relationships

Excellent continuous and uncovered exposure of the AMC extends for more than 180 m along the north side of the Kaweah River (sample location 4, Fig. 3), with more than 2000 m^2 of fresh surface for detailed observation. This spectacular exposure reveals the occurrence of granite and gabbro. Six units were identified at location 4: (1) gabbro porphyry (Kgp); (2) equigranular gabbro (Kg); (3) gabbro (Kgd); (4) white granite (Kgr); (5) medium gray granite porphyry (Kp); and (6) pegmatitic granite (Kpg). Crosscutting relationships and the nature of contacts among the first five units indicated at least two stages of intrusion (Fig. 3), and subsequent U-Pb zircon age dates (see following discussion of Zircon U-Pb Age Dating) reveal a three-stage intrusion history.

TABLE 1. MAJOR AND TRACE ELEMENT COMPOSITIONS OF ASH MOUNTAIN COMPLEX SAMPLES

Sample	10JH14	10JH15	10SQ21	10JH08	10JH01	10JH05	10JH05-2*	10JH09	10JH20	10JH21
Rock type	Diorite	Granite	Granite	Gabbro	Gabbro	Granite	Granite	Pegmatite	Gabbro	Gabbro
Location	1	1	2	3	3	3	3	3	4	4
description	Sycamore Drive	Sycamore Drive	Frys Point pluton interior, Kfp	General's Highway	General's Highway	General's Highway	General's Highway	General's Highway	Kaweah River, Unit Kgp	Kaweah River, Unit Kg
Mineralogy†	Pl, Bt, Hbl, Qz	Kfs, Pl, Qz, Bt	Kfs, Qz, Pl, Bt, Hbl	Pl, Hbl, Cpx, Bt	Pl, Hbl, Cpx, Bt	Pl, Qz, Kfs, Bt, Hbl	Pl, Qz, Kfs, Bt, Hbl	Qz, Pl, Kfs, Bt	Pl, Opx, Cpx, Hbl, Bt	Pl, Hbl, Cpx, Bt
Major elements (wt% oxide)										
SiO_2	58.67	75.03	72.61	47.76	47.27	69.70	69.66	76.91	47.76	48.69
TiO_2	0.62	0.07	0.26	1.25	1.07	0.44	0.43	0.04	1.67	1.15
Al_2O_3	16.86	13.55	14.08	17.54	20.94	14.97	15.08	13.39	17.48	17.37
Fe_2O_3	7.99	1.46	2.56	12.32	9.52	3.71	3.82	0.52	11.2	11.45
MnO	0.15	0.03	0.05	0.20	0.15	0.06	0.06	0.01	0.19	0.19
MgO	3.94	0.11	0.33	6.78	6.11	0.87	0.84	0.07	7.28	7.54
CaO	7.00	0.59	1.39	10.54	12.03	2.67	2.64	1.07	12.28	10.65
Na_2O	3.05	3.94	3.62	2.09	1.92	3.36	3.35	3.54	1.54	2.07
K_2O	1.44	4.69	4.84	0.44	0.44	3.81	3.76	4.50	0.38	0.58
P_2O_5	0.09	0.05	0.06	0.17	0.27	0.11	0.12	0.03	0.07	0.09
Total	99.81	99.52	99.80	99.09	99.72	99.70	99.76	100.08	99.85	99.78
Trace elements (ppm)										
Ni	20	nd	3	23	44	nd	3	3	27	41
Cr	18	4	8	74	86	7	7	4	129	118
V	200	5	10	295	201	26	24	4	335	337
Sc	27	5	6	45	37	10	11	3	44	40
Zn	77	41	65	97	59	80	63	17	71	80
Ga	15	16	20	18	17	18	18	16	15	17
Ba	470	1141	1132	193	1356	1501	1619	452	143	153
Rb	47	100	176	6	6	116	113	127	8	12
Th	6	10	13	4	5	12	15	18	4	3
Sr	308	50	134	454	469	270	264	94	401	388
Zr	37	81	237	72	43	227	225	59	42	57
Nb	9	6	11	9	7	15	13	10	10	8
Hf	2.3	4.0	6.8	3.1	1.3	6.8	6.5	4.1	2.1	2.6
La	16	21	31	9	5	47	47	15	7	17
Ce	26	55	69	21	14	108	102	27	12	25
Pr	3.8	5.1	7.3	2.8	2.0	10.2	10.6	4.0	2.6	4.4
Nd	12	15	25	21	5	35	33	7	11	18
Y	20	29	41	26	19	21	22	21	17	27
U	3	3	5	2	5	3	6	8	1	2
Pb	8	26	20	8	3	16	15	33	5	5
Cu	37	3	4	34	29	6	3	5	45	35

(*continued*)

TABLE 1. MAJOR AND TRACE ELEMENT COMPOSITIONS OF ASH MOUNTAIN COMPLEX SAMPLES (*continued*)

Sample	10JH18	10JH22	10JH17	10JH19	10JH16	10JH11	10SQ17	10SQ15	10SQ16
Rock type	Gabbro	Gabbrodiorite	Granite	Granite	Granite	Gabbro	Gabbro	Gabbrodiorite	Granite
Location description	4 Kaweah River, Unit Kgd	4 Kaweah River, Unit Kgd	4 Kaweah River, Unit Kp	4 Kaweah River, Unit Kp	4 Kaweah River, Unit Kgr	5 Elk Creek	6 Trail to Marble Falls	6 Trail to Marble Falls	6 Trail to Marble Falls
Mineralogy†	Pl, Hbl, Bt	Pl, Hbl, Cpx, Bt	Pl, Qz, Bt, Kfs	Qz, Kfs, Bt, Pl	Pl, Qz, Kfs, Bt	Pl, Cpx, Opx, Hbl	Pl, Hbl, Cpx, Bt	Pl, Hbl, Bt, Qz	Kfs, Qz, Bt, Pl, Hbd
Major elements (wt% oxide)									
SiO_2	50.57	54.05	70.95	71.42	72.87	47.27	50.37	54.13	71.09
TiO_2	1.06	1.42	0.35	0.34	0.25	1.52	1.59	1.22	0.33
Al_2O_3	19.62	19.99	14.86	14.6	14.11	17.14	18.67	17.85	14.40
Fe_2O_3	8.1	7.41	2.79	2.62	2.61	11.55	11.18	9.80	3.34
MnO	0.13	0.12	0.03	0.04	0.04	0.22	0.19	0.16	0.06
MgO	4.56	3.87	0.55	0.51	0.44	7.55	4.59	4.20	0.40
CaO	10.08	8.54	1.96	1.98	1.98	12.19	9.24	7.56	1.95
Na_2O	2.68	2.72	3.13	3.01	3.33	1.47	3.15	3.07	3.89
K_2O	1.22	1.48	5.00	5.11	3.99	0.18	0.59	1.58	4.15
P_2O_5	0.13	0.2	0.13	0.12	0.07	0.05	0.26	0.19	0.06
Total	98.15	99.80	99.75	99.75	99.69	99.14	99.83	99.76	99.67
Trace elements (ppm)									
Ni	20	15	nd	0	nd	10	9	17	2
Cr	53	9	7	7	11	9	5	nd	5
V	193	110	15	14	18	408	234	158	10
Sc	33	15	8	7	4	55	39	24	9
Zn	71	65	59	57	53	75	92	92	69
Ga	18	19	19	19	17	16	21	20	19
Ba	302	456	1479	1306	1402	87	287	595	1610
Rb	56	96	159	175	139	nd	12	50	109
Th	3	6	18	20	9	3	4	6	10
Sr	412	527	241	214	224	401	460	381	198
Zr	66	63	237	220	203	27	116	115	344
Nb	14	13	17	21	14	6	13	13	10
Hf	3.8	2.8	7.0	7.4	6.5	2.5	3.7	4.0	7.0
La	15	4	71	66	26	nd	19	19	42
Ce	34	22	149	144	58	4	31	42	95
Pr	4.0	1.9	14.9	13.9	6.0	1.1	4.5	4.7	9.4
Nd	20	8	46	46	14	nd	31	24	27
Y	27	17	20	21	19	10	33	28	27
U	nd	5	6	4	nd	3	3	2	6
Pb	4	9	23	22	16	6	5	8	16
Cu	24	20	4	3	8	37	29	15	9

Note: nd—not determined.

*Sample 10JH05-2 is a duplicate analysis of 10JH05.

†Mineral abbreviations after Whitney and Evans (2010): Pl—plagioclase; Bt—biotite; Hbl—hornblende; Qz—quartz; Kfs—potassium feldspar; Cpx—clinopyroxene; Opx—orthopyroxene.

Stage 1 units include Kgp, Kg, and Kgd, which are characterized by gradational and/or crenulated contacts with one another (cf. Figs. 3C, 3D), suggesting that earlier units had not completely solidified prior to intrusion of the subsequent unit. The single stage 2 unit, Kgr, displays ambiguous contacts with stage 1 units (Fig. 3C), with both relatively sharp (solid lines in Fig. 3D) and gradational (dashed lines in Fig. 3D) contacts. Stage 3 units Kp and Kpg have gradational contacts with one another. Unit Kp crosscuts (Figs. 3A, 3B) and contains stage 1 and 2 units as angular xenoliths (Figs. 3E, 3F), which suggests that stage 1 and stage 2 units had solidified prior to intrusion of stage 3 units. We collected samples of Kgp, Kgd, Kgr, and Kp from location 4 for zircon U-Pb dating.

Rock Classification and Petrography

We provide the primary mineralogy and major and trace element analyses of both AMC and nearby samples in Table 1. Figure 4 displays AMC samples from all locations (cf. Fig. 2) based on major element analyses. With one exception, the Kaweah River samples (location 4; solid symbols in Fig. 4) are classified as either gabbro or granite. The exception is a sample from stage 1 unit Kgd (10JH22), which is classified as gabbrodiorite. Another sample from this unit (10JH18) is classified as gabbro, suggesting intraunit variability. Samples from locations 1, 3, 5, and 6 are displayed as open symbols and are compositionally similar to the Kaweah River samples, with the exception of a diorite from location 1. The half-filled red diamond represents the Frys Point intrusion, which was sampled for zircon U-Pb dating and is also a granite.

AMC and local gabbros (<52 wt% SiO_2) are dominated by plagioclase and varying amounts of clinopyroxene, orthopyroxene, and hornblende with minor biotite. AMC and local intermediate rocks (~54–59 wt% SiO_2) contain plagioclase, hornblende, biotite, and either clinopyroxene or quartz. AMC and local granites contain microcline, quartz, and plagioclase with minor biotite. Some samples exhibit secondary alteration, including local replacement of biotite by chlorite and seritization of feldspars.

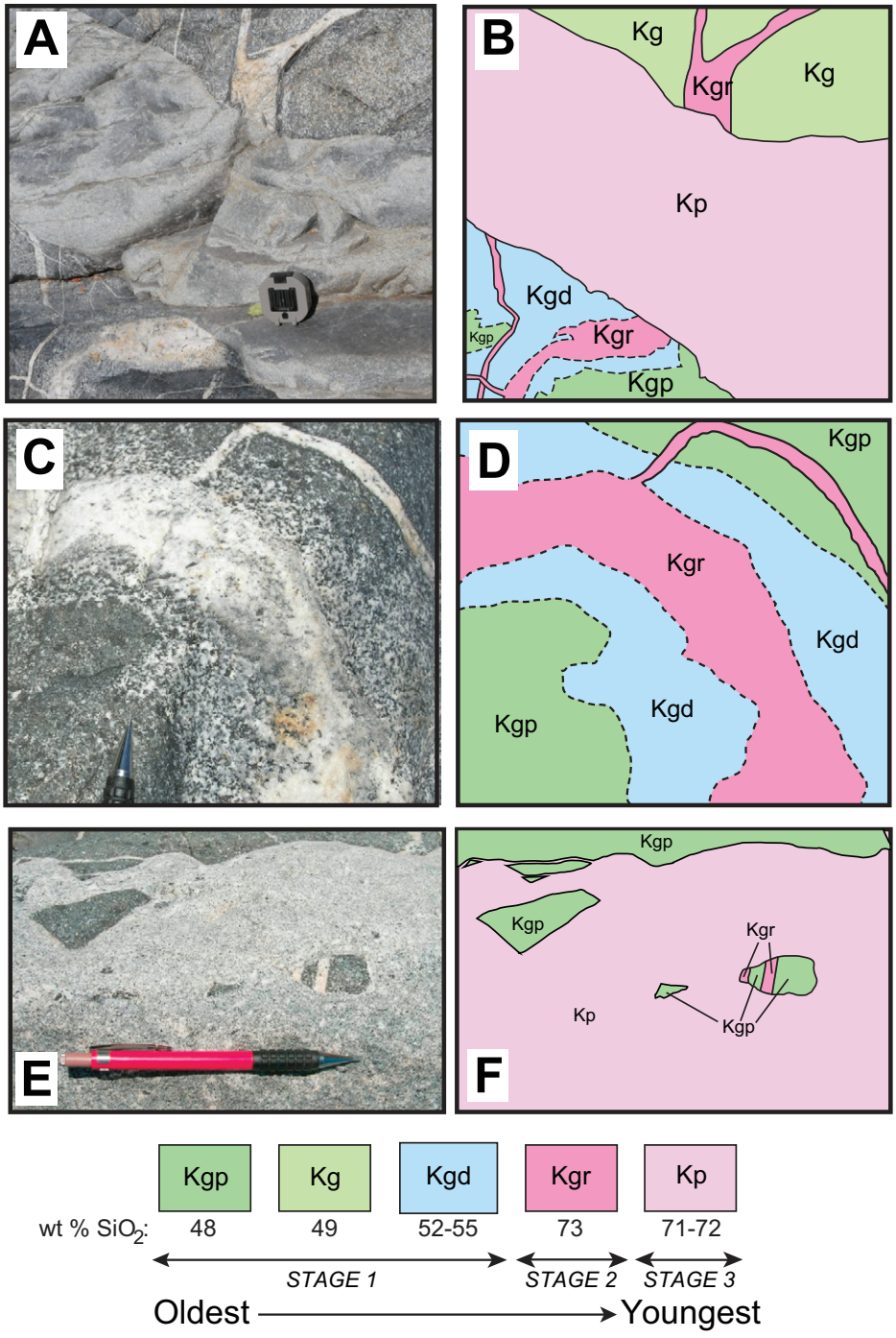

Figure 3. Field relationships of Kaweah River intrusive units Kgp, Kg, Kgd, Kgr, and Kp (Kpg is not shown) as exposed as location 4 (Fig. 2). Schematic illustrations of photos in A, C, and E are given in B, D, and F, respectively. Dashed lines in B and D represent gradational contacts. SiO_2 values (wt%) are from Table 2. Note Brunton compass and pencils for scale in A, C, and E.

Zircon Morphology

We separated and examined zircon grains using CL images for six AMC samples and the Frys Point granite; zircon morphologies for the four samples analyzed for geochronology are summarized in Table 2. CL images show that zircon grains in Kgp are dominated by sector zoning, whereas zircon grains from the other samples are dominated by concentric zoning. In granites, concentric zones become progressively narrower toward zircon grain margins. Zircon grains from granite samples often contain inherited cores, overgrowth rims, and melt inclusions.

Zircon U-Pb dating

U-Pb isotopic data for the five samples analyzed are documented in Supplemental Table 1 (see footnote 1). Gabbro samples from Kaweah River stage 1 units (10JH20, Kgp, and 10JH18,

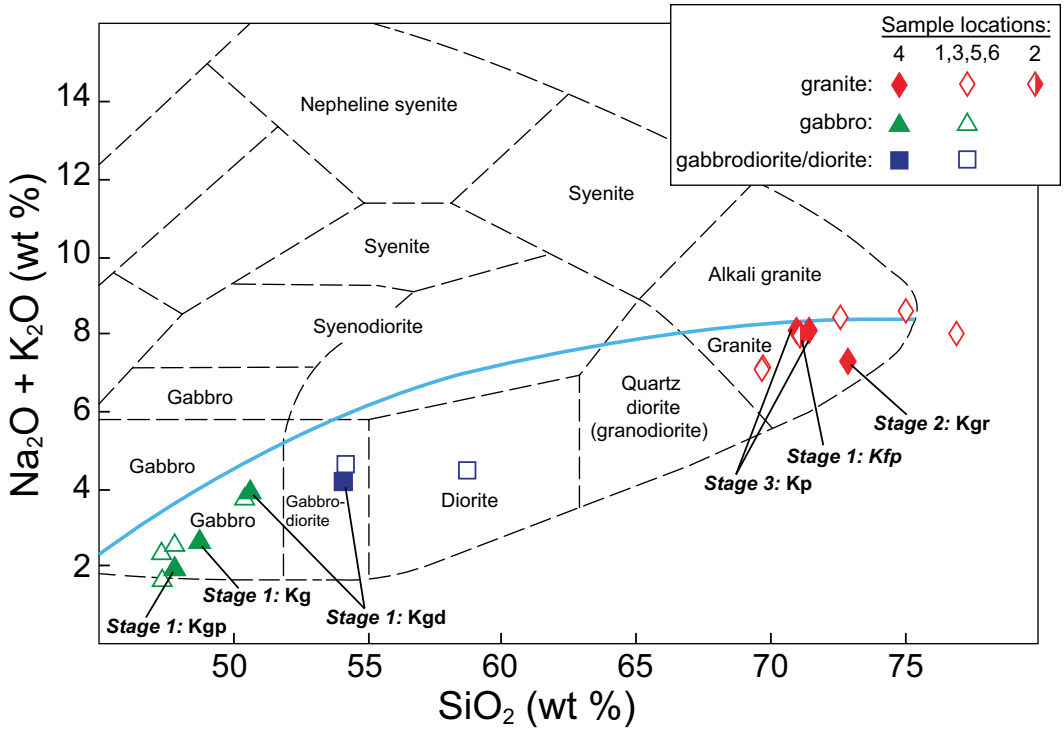

Figure 4. Ash Mountain Complex samples plotted on the total alkalis versus silica classification for plutonic rocks (Cox et al., 1979; Wilson, 1989). Open symbols represent samples taken from locations 1, 3, 5, and 6 (cf. Fig. 2). Filled symbols represent samples from the Kaweah River locality (locality 4 in Fig. 2), and the half-symbol represents a sample from location 2. Blue curve separates alkalic from subalkalic rocks.

Kgd) are dated as 105.1 ± 0.9 Ma and 105.5 ± 0.7 Ma, respectively (Fig. 5). We tentatively assign an age of 104.3 ± 0.5 Ma to stage 2 unit Kgr (10JH16) based on two concordant zircon U-Pb dates. Stage 3 unit Kp (10JH17) yields a date of 102.5 ± 0.7 Ma (Table 2; Fig. 5), suggesting a three-stage intrusion history for the AMC (Fig. 3). We also dated a granite sample from the Frys Point intrusion (10SQ21) as 105.5 Ma ± 0.7 Ma (Table 2; Fig. 5; location 2 in Fig. 2), coeval with Kaweah River stage 1 intrusions and slightly older than a published U-Pb age for the Frys Point granite (younger than 99 Ma; Chen and Moore, 1982). Dates for samples 10JH20, 10JH18, and 10SQ21 confirm that ca. 105 Ma magmatism involved coeval low- and high-silica magmas.

Zircon Trace Element Geochemistry

Trace element analyses of zircon grains collected with the SHRIMP-RG (reverse geometry) are listed in Supplemental Table 2[2]. We used these analyses to constrain crystallization temperatures and cooling rates (e.g., Barth and Wooden, 2010). Figure 6 illustrates zircon crystallization temperatures calculated using the Ti-in-zircon thermometer of Ferry and Watson (2007) plotted against Hf concentrations, because temperature-Hf relationships in zircons have been used to assess the extent of fractionation and rate of cooling within discrete magma batches (Barth and Wooden, 2010). We plot zircon grain data from four AMC units at the Kaweah River locality (stage 1 units Kg and Kgd, stage 2 unit Kgr, and stage 3 unit Kp) and a granite of the stage 1 Frys Point pluton (Kfp) from location 2 (Fig. 2). We adjusted activities of oxides (SiO_2, TiO_2) in model temperature calculations for magma compositions, as recommended by Hayden and Watson (2007), but we did not apply the pressure corrections for Ti partitioning (e.g., Ferriss et al., 2008) because we use these uncorrected model temperatures solely to evaluate relative temperature differences among samples. In the following, and in Supplemental Table 2 (see footnote 2), all temperatures listed have not been corrected for pressure.

Calculated temperatures for zircons from Kg and Kgd (gabbros) exhibit the tightest clustering. Unit Kg records the highest temperatures (748–857 °C; Supplemental Table 2 [see footnote 2]) and exhibits a relatively narrow range of Hf concentration (8755–9868 ppm), while unit Kgd records similarly high temperatures (722–830 °C) and a narrow range of Hf concentration (8971–10349 ppm). Unit Kfp (granite) records lower temperatures (670–775 °C) and a wider range in Hf concentration (8055–13099 ppm). Zircon compositions from Kgr and Kp (granites) exhibit greater scatter in temperature, but the relatively wide ranges in Hf concentration from zircon in those units (8701–13511 ppm for Kgr and 9256–14985 ppm for Kp) are similar to the range displayed by zircon from the Frys Point pluton (Kfp).

Ti-in-zircon temperatures for igneous rocks are typically lower than expected for crystallization temperatures (Fu et al., 2008). However, the relative differences between model temperatures and variations in Hf contents among AMC samples and the Frys Point granite are notable. A small change in Hf content may imply a relatively fast cooling rate because rapid cooling does not allow significant fractionation to occur (Barth and Wooden, 2010). However, samples can display different Hf-temperature trends depending on source composition and magma composition in addition to cooling rate (Wooden et al., 2007; Barth and Wooden, 2010).

The relatively small change in Hf abundance (<~1400 ppm) over their apparent crystallization temperature intervals (~110 °C) might suggest that the AMC gabbros (units Kg and Kgd) underwent little fractionation. In contrast, the large range of Hf abundances in zircons in granites from units Kfp (~5000 ppm), Kp (~5700 ppm, excluding two outliers), and Kgr (~4800 ppm) suggest significant fractionation permitted by slower cooling rates. Minimum temperatures for Kg and Kgd overlap with apparent maximum temperatures for units Kfp and Kp (Fig. 6). Although other

[2]Supplemental Table 2. SHRIMP-RG trace element data for zircons in selected AMC samples. If you are viewing the PDF of this paper or reading it offline, please visit http://dx.doi.org/10.1130/GES00890.S2 or the full-text article on www.gsapubs.org to view Supplemental Table 2.

factors can affect Hf-temperature trends, we suggest that rapid cooling (>1000 °C/m.y.; Giletti, 1986, 1991) of Kg and Kgd, inferred from their low degree of fractionation, may be explained as the result of interaction (quenching?) with coeval granitic magmas, a relationship exposed in outcrop (e.g., Fig. 3).

Whole-Rock Geochemistry

Major Elements

Major element data for the AMC and adjacent plutons are given in Table 1 and illustrated in Figure 7. For comparison, we have included ranges in elemental data from compositionally diverse (gabbro to granite) rocks across a swath of the SNB between lat 36°N and 37°N studied by Wenner and Coleman (2004) and from the El Capitan Granite (Ratajeski et al., 2005). We observe a large range of composition, from 48 to 77 wt% SiO_2, with a compositional gap between ~60 and 70 wt% SiO_2. Harker diagrams display generally linear and negative trends between SiO_2 and FeO*, MgO, Mg#, CaO, MnO, and TiO_2. Both K_2O and Na_2O increase with increasing SiO_2, with K_2O displaying a more linear trend. Al_2O_3 displays an overall negative trend with increasing SiO_2. P_2O_5 exhibits the greatest scatter with changes in SiO_2, generally increasing with increasing silica to ~55 wt% SiO_2, then decreasing with increasing silica above that value. Wenner and Coleman (2004) documented a similar range in silica content as well as trends on major element diagrams (Fig. 7), but their data display an unbroken continuum of compositions, without the compositional gap that we observe in our samples. We note that compositions of AMC granites are very similar to the El Capitan Granite (Ratajeski et al., 2005).

Trace Elements

Trace element data for AMC and local samples are given in Table 1 and illustrated in Figure 8. For comparison, we include Wenner and Coleman (2004) as the light blue shaded region on each diagram. Abundances of Ni, Cr, Sc, V, and Sr are negatively correlated with SiO_2. We observe large ranges in Ni, Cr, Sc, and V among the gabbros and diorites, whereas elemental concentrations are much more limited among the granites. In contrast, the granites exhibit wide ranges (from twofold to sixfold) in Ba, Rb, Cs, La, Ce, Th, Pb, Zr, Hf, Nb, and Y contents. Abundances of those elements generally increase with increasing silica, but some mafic and/or intermediate rocks overlap with some granites in Cs, La, Ce, Zr, Hf, Nb, and Y contents. Wenner and Coleman (2004) documented generally similar trends in trace elements (Fig. 8).

TABLE 2. U-Pb DATA AND MORPHOLOGICAL DESCRIPTIONS OF ZIRCONS IN ASH MOUNTAIN COMPLEX INTRUSIVE ROCKS

Sample	10JH20	10JH18	10SQ21	10JH17
Unit	Kgp	Kgd	Kfp	Kp
SiO2 (wt%)	~48	~52	~73	~71
Spot analyses (n)	10	12	10	11
Excluded spots (n)	None	One for discordance	One for discordance; one for high Th/U ratio	Two for high Th/U ratio
Mean age (Ma)	105.1 ± 0.9	105.5 ± 0.7	105.5 ± 0.9	102.5 ± 0.7
MSWD	0.87	0.84	1.32	1.29
Probability	0.55	0.59	0.24	0.24
Confidence with error in standard	95%	95%	95%	95%
Zircon size (μm)	~200	~200	~150	~150–400
Zircon shape	soccer ball and stubby tabular	tabular	stubby tabular	stubby tabular to elongate tabular
Zircon zoning	sector	oscillatory	oscillatory	oscillatory
Other	few melt inclusions; no inherited cores	no inherited cores	commonly contain inherited cores and melt inclusions	commonly contain inherited cores and melt inclusions
CL images				
Scale bars represent 100 μm				

Note: n—number; MSWD—mean square of weighted deviates; CL—cathodoluminescence.

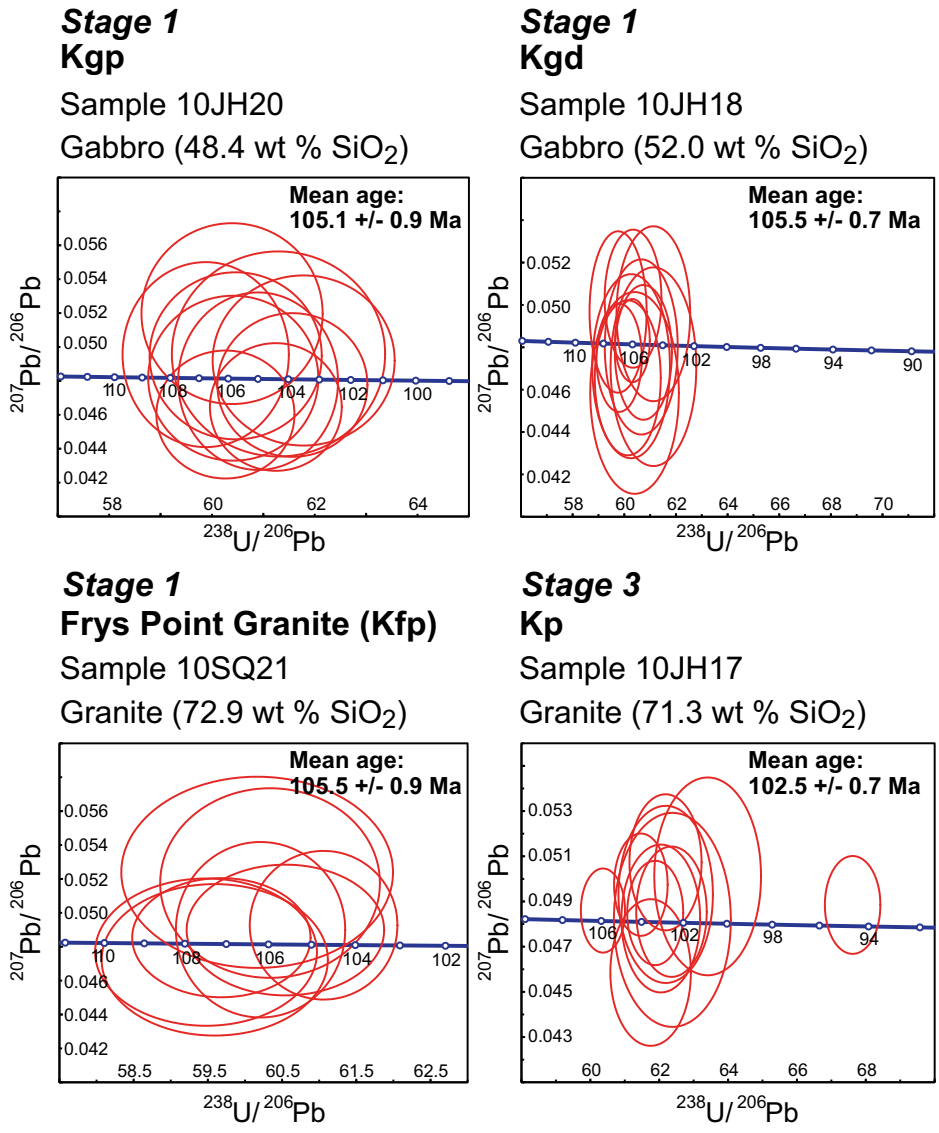

Figure 5. Concordia plots of selected stage 1 and stage 3 units (Kgp, Kgd, and Kp) from the Kaweah River site. Ellipses represent 2σ error. Also shown is a concordia plot for sample 10SQ21, from the Frys Point intrusion, which is coeval with other stage 1 units.

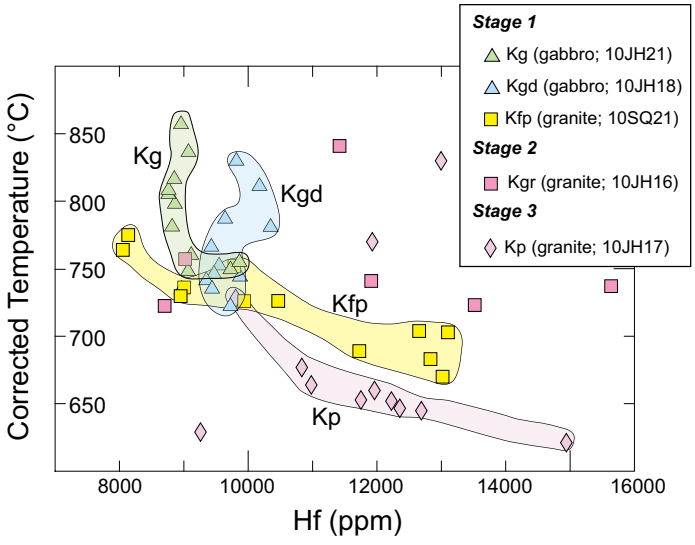

Figure 6. Ti-in-zircon model temperatures versus Hf concentrations for zircon grains in selected Ash Mountain Complex samples. Temperatures were calculated with the Ti-in-zircon thermometer of Ferry and Watson (2007). These temperatures were corrected for reduced oxide activity (TiO_2 and SiO_2) appropriate for bulk composition as suggested by Hayden and Watson (2007), but were not corrected for Ti partitioning related to pressure (e.g., Ferriss et al., 2008). See text for discussion.

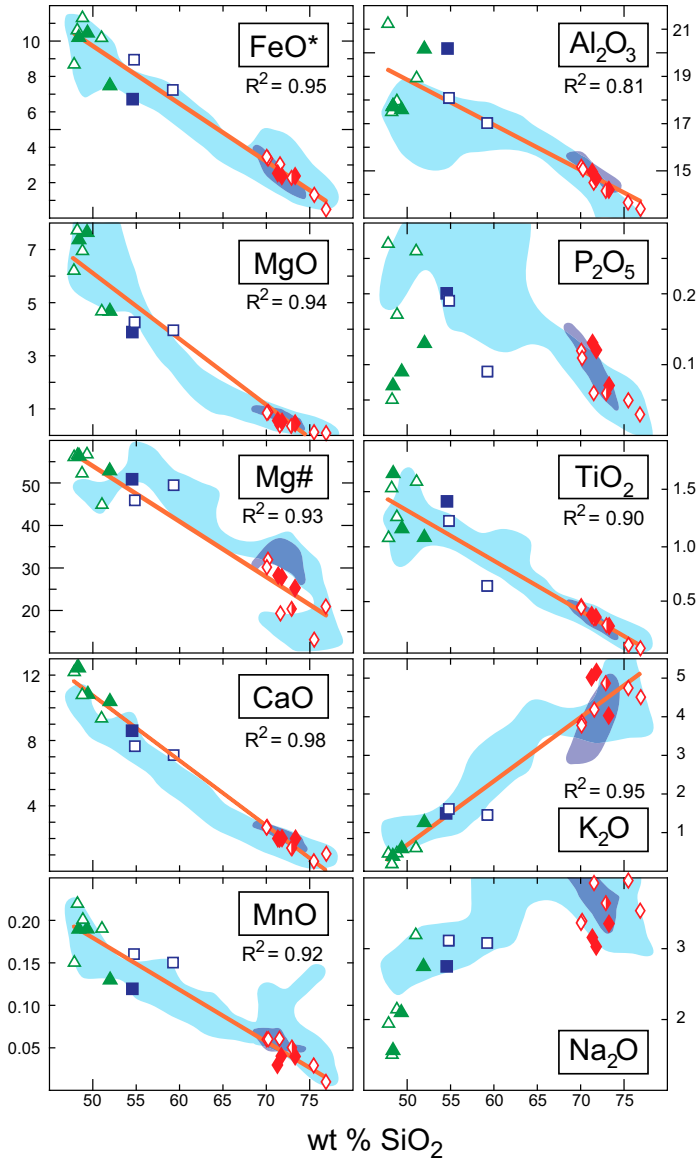

Figure 7. Harker diagrams for Ash Mountain Complex rocks. Major element data were normalized to 100% on an anhydrous basis prior to plotting. FeO* denotes total Fe as FeO (0.9 × Fe_2O_3). Mg# calculated as 100 × [(molar MgO)/(molar MgO + molar FeO*)]. Symbols as in Figure 4. R^2 denotes the correlation coefficient for linear regressions (orange lines). Light blue fields represent data for central Sierra Nevada batholith rocks documented in Wenner and Coleman (2004). Dark blue fields represent data for the El Capitan Granite (Ratajeski et al., 2005).

Sr, Nd, and Pb Isotopes

Isotopic data are given in Table 3 and illustrated in Figures 9–11. Initial isotope ratios for the seven samples analyzed (six AMC samples and one Kfp sample) range as follows: $^{87}Sr/^{86}Sr_{(i)}$ = 0.7051–0.7083; $^{143}Nd/^{144}Nd$ = 0.5123–0.5125; $\varepsilon_{Nd(i)}$ = –6.05 to –2.05; $^{206}Pb/^{204}Pb_{(i)}$ = 18.89–19.95; $^{207}Pb/^{204}Pb_{(i)}$ = 15.657–15.722; $^{208}Pb/^{204}Pb_{(i)}$ = 38.590–38.839. These values are similar to those reported by Chen and Tilton (1991) and Wenner and Coleman (2004) for the western area of their traverses of the Sierra Nevada, with western and eastern defined as those rocks west or east of the Panthalassan–North American break (Fig. 1) of Kistler (1990). Kistler (1990) defined the boundary according to isotopic shifts in granitic rocks and lithologic changes in metamorphic wall rocks. Rocks from the nearby Sequoia Intrusive Suite (Fig. 1) are plotted separately from eastern and western data fields for reference (Figs. 9–11). The Sequoia Intrusive Suite is compositionally and temporally zoned (Chen and Moore, 1982; Moore and Sisson, 1987; Hensley et al., 2010); the marginal Giant Forest granodiorite transitions into the Big Meadows granodiorite (ca. 100 Ma) and is cored by high-silica Weaver Lake granite (ca. 97 Ma). Despite compositions that include both granite and gabbros, variations in $^{87}Sr/^{86}Sr_{(i)}$ and $\varepsilon_{Nd(i)}$ ratios among AMC stage 1 samples are limited (Table 3; Figs. 9 and 10). Granite samples from stages 2 and 3 have higher $^{87}Sr/^{86}Sr_{(i)}$ ratios and lower $\varepsilon_{Nd(i)}$, relative to stage 1 rocks.

AMC samples appear to capture a transition from older rocks with $^{87}Sr/^{86}Sr_{(i)} < 0.706$ to younger rocks with $^{87}Sr/^{86}Sr_{(i)} > 0.706$ (Figs. 9 and 10). The typically spatially defined $^{87}Sr/^{86}Sr_{(i)}$ 0.706 line, which is to the west of the exposed AMC (Fig. 1), is thus a temporally expressed feature in AMC rocks. For the Fine Gold Intrusive Suite of the western SNB, exposed between 36°N and 37°N, it was shown (Lackey et al., 2012) that the $^{87}Sr/^{86}Sr_{(i)}$ 0.706 line is also a temporal feature (cf. Fig. 10) associated with a transition in magmatic style ca. 105 Ma.

Compared to data from other studies (Ratajeski et al., 2001, and references therein), stages 2 and 3 AMC rocks are along the Sr-Nd isotopic array typical of the SNB (Fig. 10), with stage 2 and stage 3 samples defining a trend toward higher $^{87}Sr/^{86}Sr_{(i)}$ and lower $\varepsilon_{Nd(i)}$. The stage 3 granite has considerably higher $^{87}Sr/^{86}Sr_{(i)}$ than is typical for SNB granitoids (Figs. 9 and 10).

With one exception (a stage 1 gabbro), Pb isotopic compositions of most AMC rocks form a fairly tight cluster within the field defined by the upper mantle of the Sierra Nevada (Fig. 11). This grouping is in contrast to other SNB suites, which largely scatter between the Sierran mantle field and the field defined by the western Great Basin basalts of presumed lithospheric mantle origin (Fig. 11). Compositions of most AMC rocks are within the area of overlap between compositions of samples from the western SNB and those of the Sequoia Intrusive Suite (Fig. 11). Viewed as a whole, there is no clear distinction in Pb isotopic compositions based on AMC rock type and the Pb data are largely ambiguous in terms of distinguishing between mantle versus crustal sources. The exception is gabbro sample 10JH18, which has a significantly higher $^{206}Pb/^{204}Pb_{(i)}$ ratio and a slightly higher $^{207}Pb/^{204}Pb_{(i)}$ ratio compared to other AMC rocks, although the $^{87}Sr/^{86}Sr_i$ (0.7057) and ε_{Ndi} (–2.3) for this gabbro are similar to other AMC gabbros (cf. Table 3).

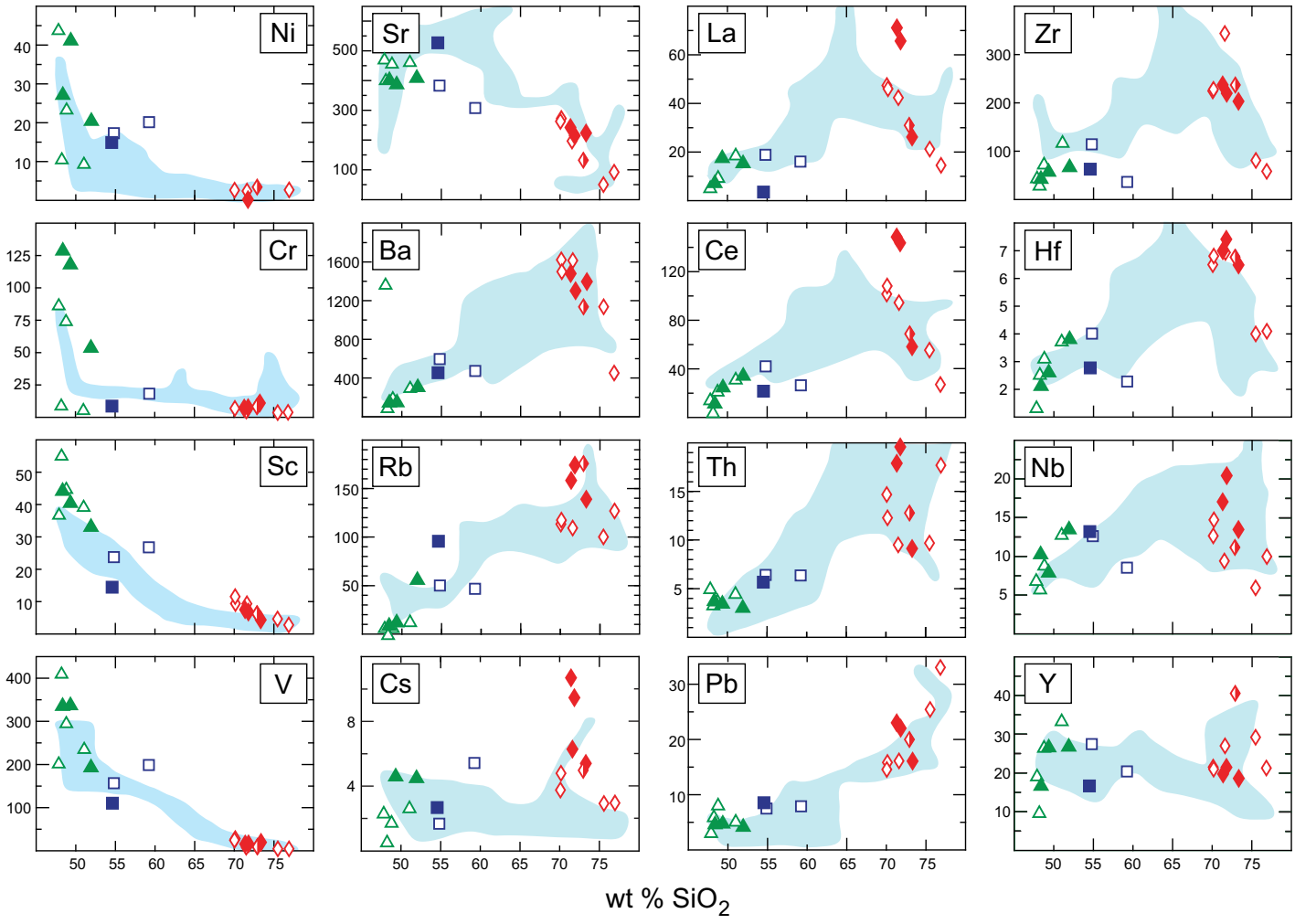

Figure 8. Abundances (in ppm) of selected trace elements versus wt% SiO_2 in Ash Mountain Complex rocks. Symbols as in Figure 4. Light blue fields represent data for central Sierra Nevada batholith rocks documented in Wenner and Coleman (2004).

TABLE 3. ISOTOPE GEOCHEMISTRY OF THE ASH MOUNTAIN COMPLEX

	10JH16	10JH17	10JH18	10JH20	10JH21	10JH22	10SQ21
Rock type	granite	granite	gabbro	gabbro	gabbro	gabbrodiorite	granite
Unit	Kgr	Kp	Kgd	Kgp	Kg	Kgd	Kfp
Age (Ma)	104.3*	102.5	105.5	105.1	105*	105*	105.5
$^{87}Sr/^{86}Sr_{today}$	0.709017 ± 6	0.711070 ± 6	0.706252 ± 6	0.705919 ± 6	0.705997 ± 6	0.706361 ± 6	0.710831 ± 6
†$^{87}Sr/^{86}Sr_i$	0.706361	0.708296	0.705668	0.705832	0.705867	0.705577	0.705145
$^{143}Nd/^{144}Nd$	0.512384 ± 5	0.512258 ± 3	0.512500 ± 4	0.512514 ± 4	0.512514 ± 4	0.512467 ± 3	0.512490 ± 4
§$^{147}Sm/^{144}Nd$	0.1027 ± 6	0.0914 ± 5	0.1670 ± 9	0.1716 ± 9	0.1693 ± 9	0.1454 ± 8	0.2108 ± 11
#$\varepsilon_{Nd(i)}$	–3.70 ± 0.10	–6.05 ± 0.07	–2.30 ± 0.09	–2.09 ± 0.08	–2.05 ± 0.08	–2.65 ± 0.08	–3.08 ± 0.10
$^{206}Pb/^{204}Pb_{today}$	19.237 ± 2	19.359 ± 2	19.952 ± 4	19.196 ± 2	19.206 ± 3	19.423 ± 1	19.217 ± 2
$^{207}Pb/^{204}Pb_{today}$	15.686 ± 2	15.703 ± 2	15.722 ± 4	15.680 ± 2	15.665 ± 3	15.697 ± 2	15.673 ± 2
$^{208}Pb/^{204}Pb_{today}$	38.892 ± 8	38.981 ± 7	38.905 ± 12	38.847 ± 8	38.797 ± 10	38.862 ± 5	38.868 ± 8
†$^{206}Pb/^{204}Pb_i$	19.237	18.978	19.952	19.143	19.087	19.119	18.886
†$^{207}Pb/^{204}Pb_i$	15.686	15.685	15.722	15.677	15.66	15.682	15.657
†$^{208}Pb/^{204}Pb_i$	38.697	38.602	38.839	38.767	38.723	38.739	38.59

Note: Analytical uncertainties are reported as ±2σ absolute standard error, indicated by variation in the last digit.

*A preliminary age of 104.3 ± 0.5 Ma for 10JH16 is based on two concordant zircon U-Pb dates and is consistent with crosscutting field relationships. Ages of 105 Ma for mafic samples 10JH21 and 10JH22 are inferred from the age for 10JH20, as field relationships indicate their coeval nature.

†$Ratio_i$ indicates ratios corrected to the U-Pb age of the rock. $Ratios_i$ for Sr and Pb are calculated using Rb, Sr, U, Th, and Pb concentrations analyzed by X-ray fluorescence (Table 2).

§Sm/Nd ratio determined by isotope dilution.

#$\varepsilon_{Nd(i)}$ calculated using $^{143}Nd/^{144}Nd_{CHUR\ today}$ = 0.512638 and $^{147}Sm/^{144}Nd_{CHUR\ today}$ = 0.1967 (CHUR—chondritic uniform reservoir) and measured Sm/Nd ratios.

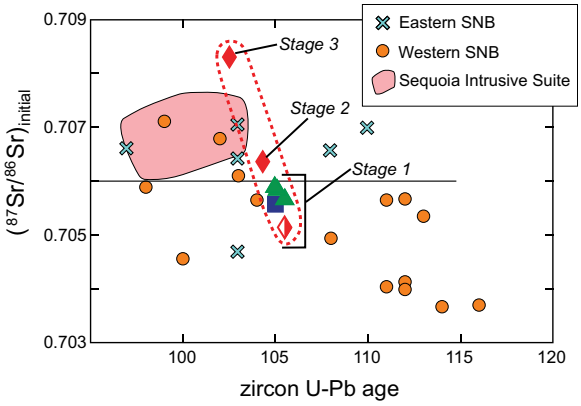

Figure 9. Initial Sr isotope compositions versus zircon U-Pb crystallization ages for Ash Mountain Complex (AMC) rocks. Red dashed curve includes AMC data; symbols as in Figure 4. Blue filled crosses represent compositions for eastern Sierra Nevada batholith (SNB) rocks (Chen and Tilton, 1991; Wenner and Coleman, 2004) and orange filled circles represent compositions from the western SNB (Chen and Tilton, 1991; Wenner and Coleman, 2004). Pink shaded field represents compositions for 14 samples of the Sequoia Intrusive Suite (Chen and Tilton, 1991; Wenner and Coleman, 2004).

DISCUSSION

Summary of Observations

AMC rocks exposed in the Kaweah River valley formed in three stages: stage 1 magmatism, ca. 105 Ma, produced granite and gabbro and/or gabbrodiorite plutons. Zircon trace element analyses suggest that the gabbros probably cooled relatively quickly, quenched by contact with cooler adjacent granites, which cooled more slowly. Stage 2 magmatism, ca. 104 Ma, and stage 3 magmatism, ca. 103 Ma, produced granitic plutons.

Major and trace element compositions of AMC and other local rocks yield trends similar to those of other central SNB granitic and gabbroic plutons, but there is a significant gap in silica composition (between ~60 and 70 wt% SiO_2) observed in the AMC. Stage 1 rocks exhibit limited ranges in isotopic compositions (Figs. 9–11) that appear to be independent of rock type and suggest derivation from isotopically similar sources. The Sr and Nd isotope characteristics are consistent with a mantle-like, relatively juvenile magmatic source for stage 1 rocks. Stage 2 and stage 3 rocks have higher $^{87}Sr/^{87}Sr_{(i)}$ and lower $\varepsilon_{Nd(i)}$ compositions compared to those of stage 1, suggesting that they had a distinct source and/or a higher degree of contamination by older continental crust (Figs. 9 and 10).

Petrogenesis of AMC Magmas

Three major processes, crystal fractionation (with or without assimilation), magma mixing, and crustal anatexis, have been proposed to play a significant role in formation of SNB magmas (Bateman and Chappell, 1979; Ratajeski et al., 2001, 2005; Sisson et al., 1996, 2005; Reid et al., 1983; Frost and Mahood, 1987; Dorais et al., 1990; Wenner and Coleman, 2004; Zeng et al., 2005; Pignotta et al., 2010; Nelson et al., 2013). Each process would generate different geochemical and isotopic signatures in the resulting rocks. To evaluate which process played the most significant role in the formation of AMC magmas, we model expected geochemical behavior for the magmatic products of each process and compare these compositions with those of AMC rocks. In our investigation of these processes, we included samples from the Kaweah River exposure of the AMC that show the clearest crosscutting relations and include other samples of similar rocks surrounding the Frys Point intrusion (Fig. 2); these additional samples are from locations 1, 2, 3, 5, and 6 (Fig. 2). In the following discussion, AMC rocks include all of these samples, unless otherwise indicated.

Trace Element Constraints on Fractionation Processes

Fractionation processes involve systematic depletion or enrichment of elements as minerals form during cooling of a parental magma (e.g., Arth, 1976). The parental magma may be a closed system undergoing fractional crystallization, such that magma composition moves in a single direction as crystallization occurs. The parental magma may assimilate new material while crystallization is occurring, such that the composition of the assimilant and the relative rates of assimilation and crystallization control changes in magma composition.

We used trace element characteristics of AMC rocks to evaluate the roles of both Rayleigh fractional crystallization and assimilation–fractional crystallization (AFC) processes in generating intermediate to felsic compositions from mafic magma. We used the composition of the most primitive AMC gabbro (sample 10JH20, based on SiO_2 and Mg#; Table 1; Fig. 7) as the parental liquid, and modeled processes until 90% crystallization was reached.

We calculated trends in incompatible trace element abundances and ratios for a variety of fractional crystallization and AFC scenarios, varying the minerals removed from the melt, the composition of the assimilant (lower crust and upper crust compositions from Rudnick and Fountain, 1995), and the relative rates of crystallization (R_c) versus assimilation (R_a; cf. Fig. 12). Mineral-melt partition coefficients (K_D values) used in the models are given in Table 4. Calculated fractional crystallization and AFC trends yield compositions that overlap with some trace element concentrations and ratios of AMC rocks (Figs. 12 and 13). For example, AFC models involving upper or lower crust provide reasonably good matches to some AMC gabbros and gabbrodiorites. By changing the parental magma to that of a gabbro with a low La/Rb ratio (La/Rb = 0.27; sample 10JH18), we would achieve a closer match to AMC gabbros and/or gabbrodiorites on the La/Rb versus Ba

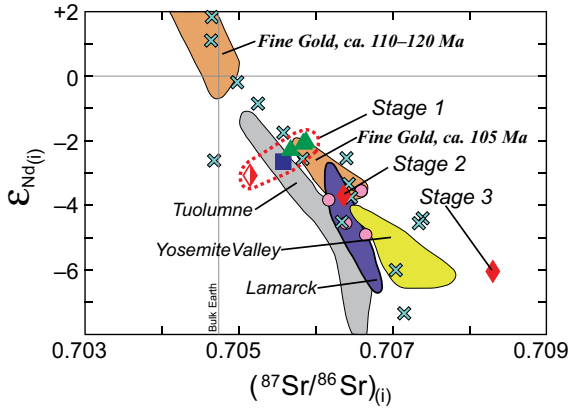

Figure 10. Initial Sr and Nd isotope compositions of Ash Mountain Complex rocks relative to other Sierra Nevada batholith (SNB) intrusive rocks. Symbols and fields as in Figures 4 and 9; U-Pb zircon ages are indicated. Orange fields indicate compositions for plutonic rocks from the Fine Gold Suite (Lackey et al., 2012). Pink filled circles represent compositions of the Sequoia Intrusive Suite. Also shown are compositional fields for other SNB plutonic rock suites as given by Ratajeski et al. (2001, and references therein), including the Tuolumne Intrusive Suite, the Lamarck Granodiorite, and the Yosemite Valley Intrusive Suite.

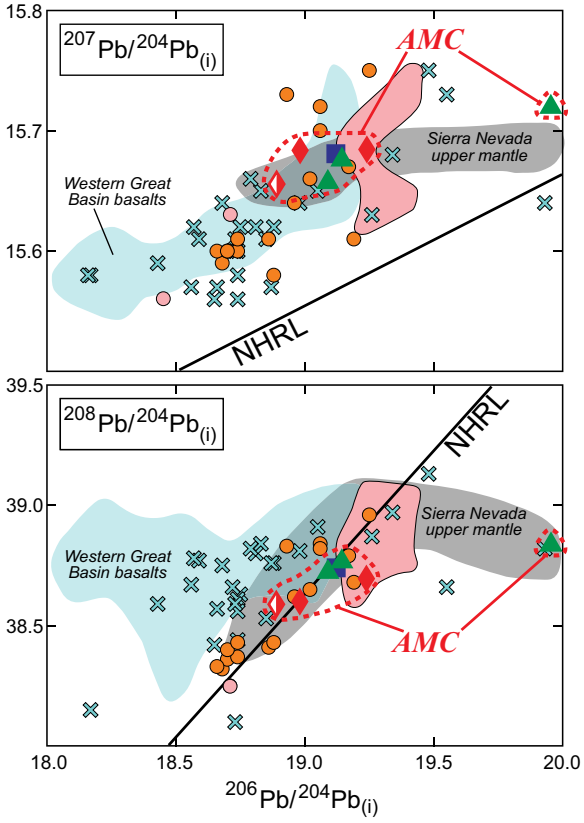

Figure 11. Initial $^{207}Pb/^{204}Pb$ and $^{208}Pb/^{204}Pb$ ratios versus $^{206}Pb/^{204}Pb$ ratios for selected Ash Mountain Complex (AMC) samples and other Sierra Nevada batholith intrusive suites. Symbols as in Figures 4 and 9. The pink field and pink filled circles represent compositions of the Sequoia Intrusive Suite. Also shown are fields for western Great Basin basalts and Sierra Nevada upper mantle as given by Wenner and Coleman (2004, and references therein). NHRL is the Northern Hemisphere reference line of Hart (1984).

diagrams. However, the models do not satisfactorily produce the trace element characteristics of AMC granites, in particular, the high (>10) Zr/Nb ratios and high abundances of Ba and Rb. The ranges in some incompatible trace element ratios (e.g., La/Rb and Nb/Y; Figs. 13 and 14) for AMC gabbros suggest derivation from mantle sources with variable trace element signatures, but none of the gabbros appear to be feasible parental magmas to AMC granites.

Trends calculated for fractional crystallization and AFC processes (Figs. 12 and 13) are simplistic because changes in the fractionating mineral assemblage with increasing differentiation were not taken into account. For example, with progressive differentiation toward dacitic compositions, biotite might appear. Biotite has high distribution coefficients for Ba and Rb (e.g., Arth, 1976) and removal of biotite would result in depletions in Ba and Rb in the remaining magmas, making it even more difficult to explain the high Ba and Rb concentrations observed in AMC granites (Fig. 12). Thus, the high Ba and Rb concentrations observed in the AMC granites (Fig. 12) suggest that crystal fractionation, with or without assimilation, did not play a significant role in generating AMC felsic magmas. Although concentrations of incompatible trace elements in granitic magmas are sensitive to the involvement of accessory minerals during fractionation processes, the observed ranges in some incompatible trace element ratios (Zr/Nb, Ce/Nb, Zr/Y, and Nb/Y; Figs. 13 and 14) suggest that AMC felsic rocks were not generated from a single parental magma. To summarize, while upper crustal contamination is permissive of a genetic relationship among AMC gabbros and gabbrodiorites, this process cannot account for the high concentrations or wide ranges of incompatible trace element concentrations in the felsic rocks.

Magma Mixing

Mixing between felsic and mafic end members has been proposed as an origin for intermediate magmas of the SNB (e.g., Reid et al., 1983; Frost and Mahood 1987; Dorais et al., 1990; Sisson et al., 1996; Ratajeski et al., 2001; Wenner and Coleman, 2004; Pignotta et al., 2010). Mixing of the isotopically similar stage 1 gabbroic and granitic magmas would produce hybrid magmas with similar isotopic compositions; this is observed for stage 1 gabbrodiorite (sample 10JH22, Table 3). The largely linear trends observed for most major elements in AMC intrusive rocks (Fig. 6) are also consistent with an origin via mixing; however, the large compositional gap (between ~60 and 70 wt% SiO_2) suggests that magma mixing did not play a major role in the petrogenesis of AMC magmas. Compositional gaps can be the result of crystal fractionation (e.g., Brophy, 1991; Dufek and Bachmann, 2010), but the lack of mingling textures in the AMC also does not support mixing processes. This is in contrast to other suites in the SNB that contain numerous occurrences of intermediate rocks and spectacular examples of mingling textures in mafic enclaves and swarms in granodiorites, interpreted as the result of interaction between mafic and felsic end members (Barbarin, 1990, 1991; Dorais et al., 1990; Wenner and Coleman, 2004).

Intermediate rocks studied by Wenner and Coleman (2004) exhibit significant ranges in trace elements such as La, Zr, Ba, Ce, Hf, Th, and Nb (Fig. 8) that could be the result of the involvement of multiple felsic mixing end members exhibiting a wide range in those elements. Both the granites studied by Wenner and Coleman (2004) and the AMC granites (Fig. 8) exhibit wide ranges in those trace elements. Although felsic magmas apparently did not mix with mafic end members to generate intermediate rocks in the AMC, AMC felsic rocks could represent potential end-member compositions involved in the origin of other SNB intermediate rocks.

Isotopic Constraints on Mixing Processes

We used isotopic modeling to evaluate the relative roles of mantle and crustal sources in generating AMC magmas. We started with simple mixing models because trace element models ruled out the importance of AFC processes in generating AMC granitic magmas. In addition, AFC models typically require unrealistic amounts of fractionation and assimilation as well as impractical mineral-melt distribution coefficients to account for isotope arrays in Sierran granitoid rocks (e.g., Kistler et al., 1986; Lackey et al., 2012). Studies of plutons and their adjacent wall-rock contacts show minimal local assimilation (Mills et al., 2009; Lackey et al., 2012), including contacts within the lower crust (Saleeby et al., 2008), diminishing the probable role of assimilation processes even further. Magma mixing was unlikely to have played a major role in the petrogenesis of the AMC because of the absence of textural and compositional intermediate hybrids, but source rocks could have mechanically mixed prior to melting. Thus, isotopic mixing models may provide constraints regarding how source rocks that produced stage 1 AMC magmas are related to sources that produced stage 2 and 3 magmas, which have higher Sr_i and lower ε_{Nd}.

Our mixing models for Sr and Nd isotopes (Fig. 15) illustrate possible contributions of crust and mantle reservoirs to AMC magmas. Table 5 provides Sr-Nd data for each reser-

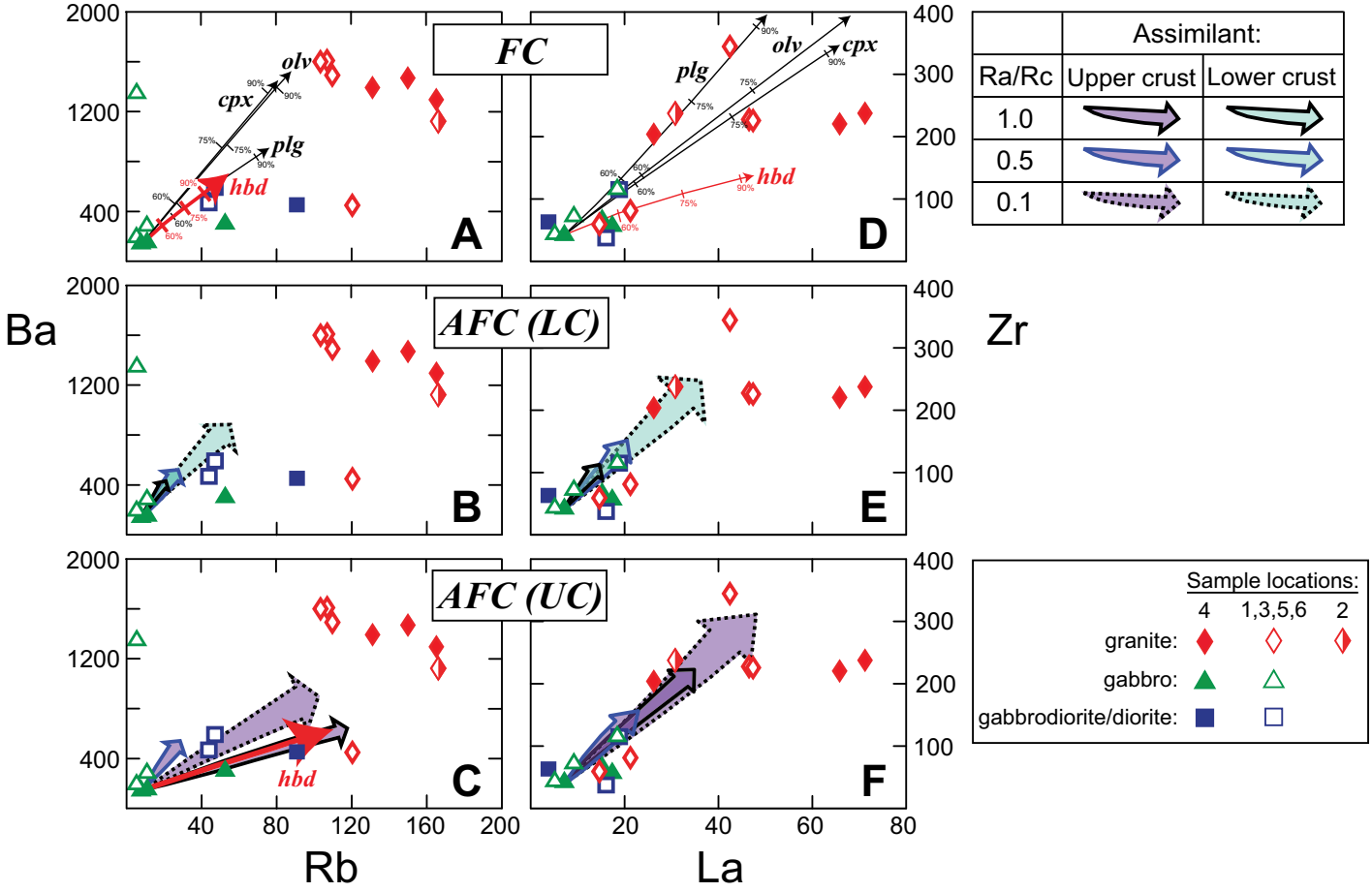

Figure 12. Trace element compositions of Ash Mountain Complex rocks and calculated trends for fractional crystallization (FC) and assimilation plus fractional crystallization (AFC) models. (A–C) Ba (ppm) versus Rb (ppm). (D–F) Zr (ppm) versus La (ppm). Symbols as in Figure 4. Mineral-melt distribution coefficients used in the models are given in Table 4. Arrows in A and D represent closed system Rayleigh FC processes involving olivine (olv), plagioclase (plg), clinopyroxene (cpx), or hornblende (hbd). Tick marks are shown for 60%, 75%, and 90% crystallization. In A, the hornblende fractionation trend is shown in red to distinguish it from the trend for plagioclase fractionation. Trends designated by arrows in B, C, E and F are for AFC processes, calculated using the equation given by DePaolo (1981). Except for C, each AFC trend encompasses individual vectors for removal of olivine, clinopyroxene, plagioclase, or amphibole to 90% crystallization (closed system equivalent). In C, the purple shaded arrows include individual vectors for removal of olivine, clinopyroxene or plagioclase, and the red arrows represents removal of hornblende; all trends represent to 90% crystallization (closed system equivalent). The narrow and broad red arrows represent rate of assimilation/rate of crystallization (Ra/Rc) 0.1 and from 0.5 to 1.0, respectively. See legend for the composition of the assimilant (either lower or upper crust [LC, UC]; from Rudnick and Fountain, 1995) and assumed Ra/Rc.

voir considered. The lithospheric mantle value of Kistler et al. (1986) is adopted as the end-member reservoir because even the most mafic rocks in the western Sierra (e.g., olivine gabbros in the western foothills) give little indication of an asthenospheric, depleted-mantle source (Clemens-Knott, 1992). Instead, Sierran mantle contributions appear to be primarily subarc lithospheric mantle (Menzies et al., 1983; Coleman et al., 1992; Lee et al., 2000). Crustal reservoirs shown in Figure 15 include the Sierran crustal value of Kistler et al. (1986), and upper and lower crustal basement of the ca. 1.7 Ga Mojave province (Miller et al., 2000). Also shown are average isotopic compositions for pyroxenite xenoliths and plagioclase-bearing granulite xenoliths of the SNB (Mukhopadhyay and Manton, 1994; Ducea, 2002); Kings Sequence schist from a migmatite complex in the southern Sierra (Zeng et al., 2005); individual analyses of Mojave crustal rocks (Newberry and Hill-3478; Martin and Walker, 1992); and individual analyses of a Precambrian schist (PC30a) and a Sierran crustal xenolith (Big Creek, B37) (Kistler and Fleck, 1994).

Trends are shown (Fig. 15) for mechanical mixing of Sierran lithospheric mantle with Sierran crust (gray curve), ca. 1.7 Ga Mojave lower crust (blue curve), and a highly radiogenic Mojave crustal sample (black curve). Also shown is a mixing trend (green dashed curve) between the AMC gabbro with the lowest $^{87}Sr/^{86}Sr_i$ and highest ε_{Ndi} (sample 10JH18, cf. Table 3) and a lower crustal xenolith from Big Creek in the central SNB.

Stage 1 AMC rocks occupy positions along mixing lines that suggest sources containing ~40% or 20% of Sierran or Mojave lower crust, respectively (Fig. 15). The stage 2 granite also is along the mixing curve between lithospheric mantle and Mojave lower crust, but requires more crust in the source. If the lithospheric mantle was of a more enriched nature (e.g., Coleman et al., 1992), less crust would be required to generate both stage 1 and *2* magmas.

TABLE 4. PARTITION COEFFICIENTS FOR TRACE ELEMENT MODELING

Coefficients used in FC and AFC models*				
	plagioclase	clinopyroxene	hornblende	olivine
Ni	0.04	7.75	6.8	17.45
Cr	0.05	34	17	0.7
K	0.17	0.038	0.96	0.007
Cs	0.025	0.01	0.01	0.001
Ba	0.23	0.026	0.42	0.01
La	0.17	0.052	0.2	0.001
Nd	0.08	0.31	0.045	0.007
Zr	0.048	0.1	0.5	0.012
Hf	0.051	0.263	0.5	0.013
Y	0.03	0.9	1.2	0.01
Sr	1.8	0.06	0.46	0.014
Rb	0.07	0.031	0.29	0.006
Nb	0.01	0.005	0.8	0.01
Th	0.01	0.03	0.25	0.01
Coefficients used in batch partial melting models†				
	plagioclase	clinopyroxene	hornblende	garnet
Sr	1.840	0.300	0.720	0.013
Y	0.005	1.235	1.560	16.000
	quartz	k-feldspar	biotite	orthopyroxene
Sr	0.020	4.000	0.200	0.001
Y	0.020	0.020	0.030	0.161

Note: Most values are from the compilation of Rollinson (1993, and references therein). The exceptions are coefficients for Sr and Y in plagioclase, clinopyroxene, hornblende, garnet, and orthopyroxene, which are from Hoffman et al. (2011, Supplementary Data 5, and references therein).

*Fractional crystallization (FC) and assimilation–fractional crystallization (AFC); illustrated in Figures 12 and 13.

†Illustrated in Figures 20 and 22.

The stage 3 granite is along the mixing trend between the AMC gabbro and Big Creek lower crustal xenolith. This trend could represent mixing of magmas with the isotopic characteristics of these end members. However, with a silica content of ~71 wt%, it is unlikely that the stage 3 granite (10JH16, cf. Table 3) is an ~45:55 mix of felsic melt (with ~70–75 wt% SiO_2) and mafic magma (with ~50 wt% SiO_2). Instead of magma mixing, we suggest that this granite was derived by melting a source containing crust that is isotopically distinct from the source or sources of stage 1 and *2* magmas. Alternatively, the source could have been similar to average Sierran granulite xenoliths (cf. Fig. 15).

Previous oxygen isotope mass balance calculations show that SNB magmas typically contain 5%–20% crust (Lackey et al., 2005, 2008, 2012), with as much as 35% in some western SNB tonalites (Lackey et al., 2012). This upper limit of crustal input is similar to the 20%–30% proportion suggested by the Sr-Nd mixing trend using Mojave lower crust reservoir and less than the ~40% proportion of Sierran crust suggested for AMC stage 1 magmas. If a significant crustal component was involved in AMC magma genesis, $\delta^{18}O$ crustal values would be relatively low. For example, Sierran pyroxenite xenoliths plot at ~50:50 mixture of Sierran mantle and crust. Upper crustal $\delta^{18}O$ values of 14.5‰ are based on measurements of SNB wall rocks (Lackey et al., 2006). A mixture of 50% Sierran mantle with a $\delta^{18}O$ value of 6.0‰ (Kistler et al., 1986), and 50% upper crust with a $\delta^{18}O$ of 14.5‰ produces $\delta^{18}O$ values of 10.25‰ in the derived magma, higher than the observed 7.2‰ reported for pyroxenite xenoliths (Ducea, 2002; Lackey et al., 2005). However, use of a lower crustal $\delta^{18}O$ of 8.5‰ results in a perfect match. Considering oxygen isotope systematics in the SNB (Lackey et al., 2005, 2006, 2008, 2012), we thus propose that the dominant crustal input to AMC sources is mafic lower crust. For rocks with $^{87}Sr/^{86}Sr_i$ values >0.706, such mafic lower crust has Proterozoic model ages of 1.7–1.8 Ga (e.g., DePaolo, 1981; Kistler et al., 1986; Chen and Tilton, 1991). For rocks with $^{87}Sr/^{86}Sr_i$ <0.706, such mafic crust may also include portions of Paleozoic accreted terranes (e.g., Saleeby, 2011).

To summarize, the Nd and Sr isotopic characteristics of AMC rocks suggest modest (~20%–40%, perhaps less, depending on the degree of enrichment of lithospheric mantle) crustal input into ca. 105 Ma stage 1 AMC magma sources. There is little isotopic variation among stage 1 rocks, suggesting a common source, which we propose is mafic crust. Both stage 2 and 3 granites appear involve a greater crustal component compared to stage 1 granite. The stage 3 granite appears to be derived from a distinct crustal source, which was tapped after 104 Ma.

Crustal Anatexis

Partial melting of continental crust may be an important process in generating felsic SNB magmas (Hildreth and Moorbath, 1988; Beard and Glazner, 1995; Ducea, 2001; Petford and Gallagher, 2001; Wenner and Coleman, 2004). This partial melting is presumably triggered by intrusion and stagnation of juvenile, mantle-derived mafic magmas (e.g., Hildreth, 1981; Bergantz, 1989). To investigate the potential role of partial melting in the production of AMC granites, we compare major element compositions of AMC granites to a wide variety of experimentally produced partial melt compositions derived from mafic to intermediate crustal sources (Fig. 16).

Natural mafic starting compositions with <~1.0 wt% K_2O yield melts (gray shaded region, Fig. 16) with K_2O contents that are lower than those in AMC granites; this observation is consistent with other studies on SNB batholiths (Sisson et al., 2005; Ratajeski et al., 2005). Figure 16 also illustrates compositions of synthetic glasses produced in partial melting experiments that involve a variety of natural materials considered to be important in the generation of high-K, granitic magmas associated with continental arcs (Skjerlie and Johnston, 1993, 1996; Skjerlie and Patiño-Douce, 2002; Patiño-Douce, 2005; Ratajeski et al., 2005; Castro et al., 2010). Figure 16 summarizes the parameters of these experimental studies. Starting compositions include low-K mafic sources (Skjerlie and Patiño-Douce, 2002), medium- to high-K mafic sources (Ratajeski et al., 2005), intermediate (tonalitic to dioritic) sources (Skjerlie and Johnston, 1993, 1996; Patiño-Douce, 2005), and mechanical mixtures of mid-oceanic ridge basalt plus sediment (Castro et al., 2010). All of these experiments yield compositions that overlap those for the AMC. Some glasses (filled orange diamonds, Fig. 16) produced from the low K_2O sources of Skjerlie and Patiño-Douce (2002) are within the range of AMC compositions, but most (open orange diamonds) have compositions with significantly lower K_2O; therefore, we do not consider this latter group further.

The best potential match for the experimental partial melt granite would be the least evolved granites (LEGs), which have not undergone subsequent crystal fractionation. In an attempt to identify LEGs in the AMC, Ba and Sr abundances were calculated for Rayleigh fractional crystallization and compared to observed Ba and Sr concentrations in AMC granites. Ba and Sr are among the few trace elements whose concentrations are largely controlled by major phases (potassium feldspar, plagioclase, biotite, hornblende) rather than accessory phases (apatite, zircon), which have very large K_D values for other trace elements (e.g., rare earth elements, Zr, Hf). Figure 17 illustrates fractionation trends assuming a range of Ba and Sr bulk distribution coefficients appropriate for granitic melts (cf. Rollinson, 1993). Three of the AMC granites with high silica contents (73–77 wt%) are along

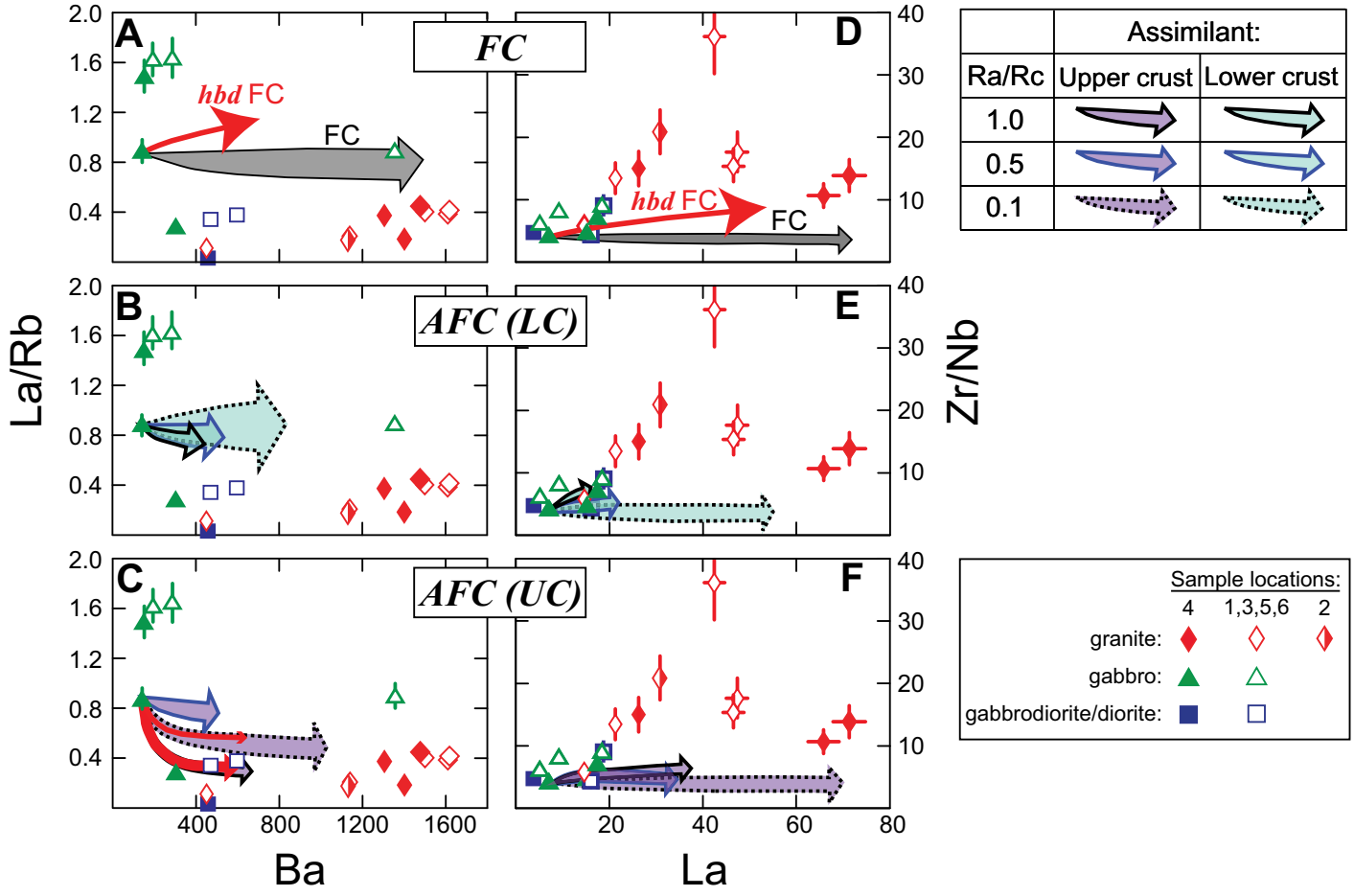

Figure 13. Trace element compositions of Ash Mountain Complex rocks and calculated trends for fractional crystallization (FC) and assimilation plus fractional crystallization (AFC) models. (A–C) La/Rb versus Ba (ppm). (D–F) Zr/Nb versus La (ppm). Symbols as in Figure 4. Mineral-melt distribution coefficients used in the models are given in Table 4. Analytical uncertainties for each trace element or ratio are represented by error bars. Gray shaded arrows in A and D labeled FC represent closed system FC processes involving olivine, plagioclase, or clinopyroxene. The length of the arrow represents as much as 90% crystallization. The red arrows in A, C, and D represent hornblende fractionation with the lengths representing as much as 90% crystallization. Trends designated by arrows in B, C, E, and F are for AFC processes, calculated using the equation given by DePaolo (1981). Each AFC trend encompasses individual vectors for removal of olivine, clinopyroxene, plagioclase, or amphibole to 90% crystallization (closed system equivalent). See legend for the composition of the assimilant (either lower or upper crust [LC, UC]; from Rudnick and Fountain, 1995) and rate of assimilation/rate of crystallization (Ra/Rc).

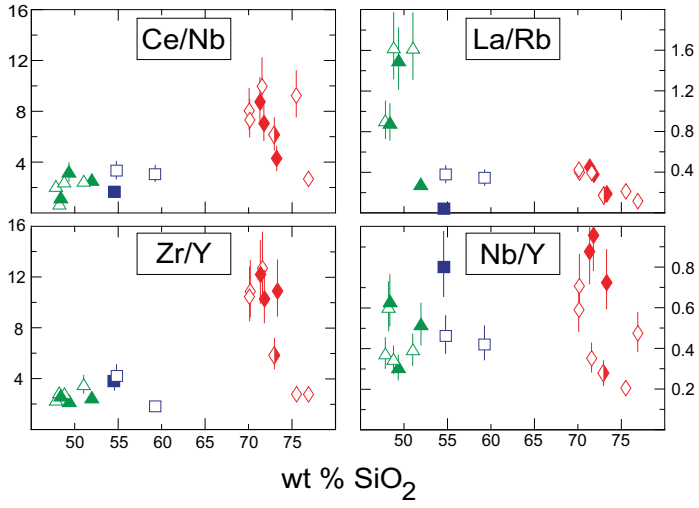

Figure 14. Selected incompatible trace element ratios plotted versus wt% SiO_2 for Ash Mountain Complex intrusive rocks. Analytical uncertainties are represented either by the size of the symbol or error bars.

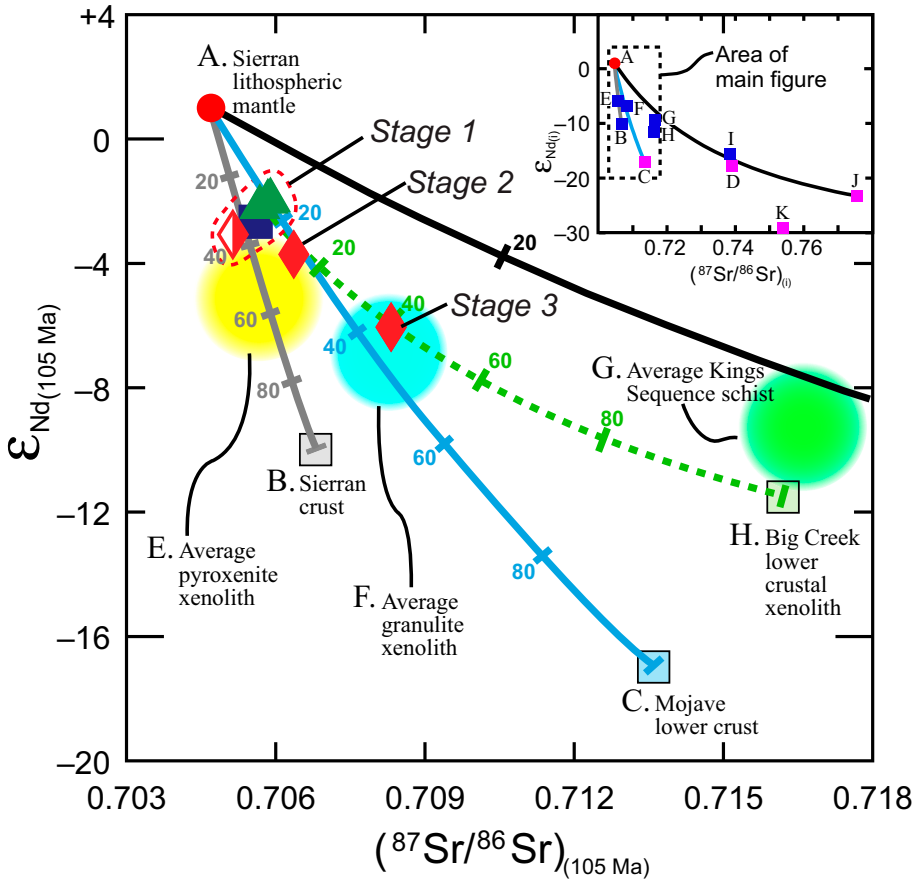

Figure 15. Mixing models for Nd and Sr isotopes; symbols as in Figure 4. Mixing parameters and reservoirs are given in Table 5. Inset illustrates Nd and Sr compositions for all reservoirs listed in Table 5 and mixing curves between Sierran lithospheric mantle (Kistler et al., 1986) and selected crustal reservoirs. Pink squares in inset represent materials from ca. 1.7 Ga Mojave crust (reservoirs C, D, K, and J; cf. Table 5). The main figure shows the Nd-Sr compositions of Ash Mountain Complex rocks. Mixing curves from the inset are also shown in the main figure (denoted by dashed black rectangle in inset). The gray curve represents mixing with typical Sierran crust (reservoir B, Kistler et al., 1986). The blue and black curves represent mixing with two different materials representing Mojave lower crust (reservoir C, Miller et al., 2000; reservoir J, Martin and Walker, 1992). Also shown in the main figure is a mixing curve (green dashed curve) between stage 1 gabbro (10JH18) and lower crust represented by the Big Creek lower crustal xenolith (reservoir H, Kistler and Fleck, 1994). Colored spheres represent average compositions of Sierran pyroxenite and granulite xenoliths (reservoirs E and F, Ducea, 2002; Mukhopadhyay and Manton, 1994), and Kings Sequence schist (reservoir G, Zeng et al., 2005).

TABLE 5. MIXING PARAMETERS USED FOR STRONTIUM-NEODYMIUM ISOTOPE MODELING

	Reservoir	Sr (ppm)	Nd (ppm)	$^{87}Sr/^{86}Sr_{(t)}$*	$\varepsilon_{Nd(t)}$
A	Sierran lithospheric mantle	555[1]	24[1]	0.7047[1]	1.0[1]
B	Sierran crust	475[1]	19[1]	0.7068[1]	–10.0[1]
C	Mojave lower crust	412[2]	24[2]	0.7136[2]	–17.0[2]
D	Mojave upper crust	216[2]	48[2]	0.7390[2]	–18.0[2]
E	Average Sierran pyroxenite xenolith	91[3]	7[3]	0.70569[3]	–6.0[3]
F	Average Sierran granulite xenolith	363[3,4]	17[3,4]	0.70827[3,4]	–6.8[3,4]
G	Average Kings Sequence schist	219[5]	39[5]	0.71661[5]	–9.3[5]
H	Big Creek lower crustal xenolith (B37)	186[6]	39[6]	0.7162[6]	–11.5[6]
I	Precambrian schist (PC30a)	164[6]	47[6]	0.7383[6]	–15.6[6]
J	Mojave (Newberry)	199[7]	112[7]	0.77546[7]	–23.3[7]
K	Mojave (Hill 3478′)	229[7]	40[7]	0.75395[7]	–29.2[7]

Note: Reservoir letters A–K represent various isotopic reservoirs used in isotopic mixing models illustrated in Figure 15. Data sources: 1—Kistler et al. (1986); 2—Miller et al. (2000); 3—Ducea (2002); 4—Mukhopadhyay and Manton (1994); 5—Zeng et al. (2005); 6—Kistler and Fleck (1994); 7—Martin and Walker (1992).
*Initial ratios recalculated for time, t = 105 Ma.

these trends and are considered to be evolved from AMC granites with lower silica contents (~70–71 wt%); they are thus are not included in subsequent figures.

CIPW-normative ternary diagrams (Fig. 18) and Harker diagrams (Fig. 19) compare compositions of the melts produced in experiments listed in Figure 16 against compositions of AMC LEGs. All data sets overlap the compositions of AMC rocks to varying degrees. Given uncertainties in synthetic glass compositions (cf. Fig. 18), these data do not compel us to rule out any particular set of experiments. However, with the exception of TiO_2 (Fig. 19), the melts generated by Ratajeski et al. (2005) appear to be the best fit. The compositions of these glasses have the most overlap with AMC granites and exhibit similar decreases in Al_2O_3 with increasing silica, as observed for AMC granites (Fig. 19). Although the melts generated by Ratajeski et al. (2005) display slightly higher Al_2O_3 values for given SiO_2 values, the majority of synthetic glasses from other experiments display significantly higher Al_2O_3 abundances than AMC granites.

During anatexis, the residual source mineralogy strongly influences the trace element compositions of the derived melts (e.g., Martin, 1987; Drummond and Defant, 1990; Rapp et al., 1991; Johnson et al., 1997; Hoffmann et al., 2011). For example, melts derived from garnet-bearing mafic sources have low Y but high Sr/Y values because of the high K_D for Y (~16; Martin, 1987) and low K_D for Sr (~0.01; Martin, 1987) for garnet. In contrast, melts derived from garnet-free amphibolite sources have low Sr/Y because of residual plagioclase, which has a low K_D for Y (~0.60; Martin, 1987) and moderate K_D for Sr (~2; Martin, 1987). In the experiments used in our evaluation of AMC LEGs (Fig. 16), those run at pressures higher than 10 kbar include garnet in the residue, whereas lower pressure experiments do not.

To evaluate the role of residual source compositions on Sr and Y abundances in AMC LEGs, these elements were modeled using the batch melting model of Shaw (1970). Sr and Y abundances in partial melts produced in five of the six experiments listed in Figure 16 were calculated using mineral modes in the residue and percentage of coexisting glass. The exception is the study of Skjerlie and Patiño Douce (2002; see following). Table 4 gives K_D values used in the models, Table 6 provides the model parameters, and Table 7 provides references for the source compositions assumed in the models. Whenever possible, we used Sr and Y contents provided for the experimental starting materials (e.g., Ratajeski et al., 2005; Castro et al., 2010). If those data were not available, we used a range

A

Source	Starting material(s) SiO_2	Starting material(s) K_2O	Symbol	Temp (°C)	Pres (kbar)	Residual garnet?
Skjerlie and Johnston, 1993	~54	~1.2		975 to 1050	10	No
Skjerlie and Johnston, 1996	~59	~1.6		875 to 975	10 to 20	Yes
Skjerlie and Patiño-Douce, 2002	~50	~0.14		1025 to 1075	27 to 32	Yes
	~50	~0.14		1025 to 1075	27 to 32	Yes
Patiño-Douce, 2005	~61.5	~2.6		940 to 1150	15 to 32	Yes
Ratajeski et al., 2005	~51	~1.0		825 to 850	7	No
	~51	~2.3				
	~54	~1.2				
Castro et al., 2010	~70	~3.9		1000 to 1100	15 to 20	Yes
	~60	~2.0				
	~65	~2.9				

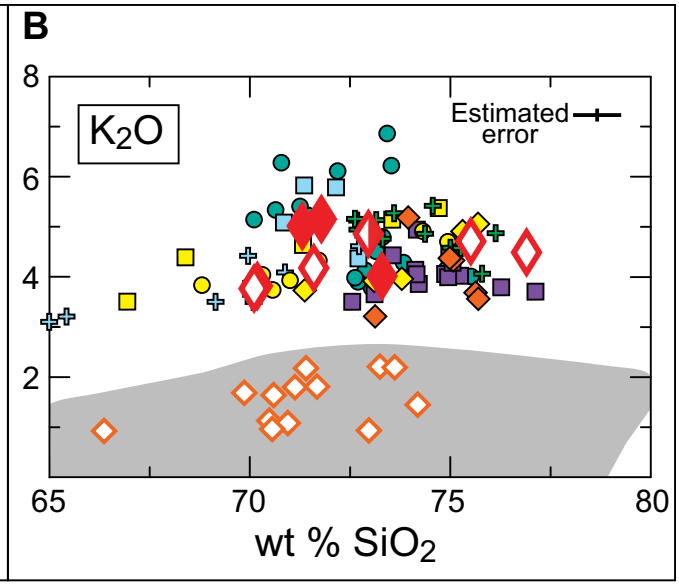

Figure 16. (A) Summary of partial melting experiments involving a variety of starting materials, generating compositions that are reasonable matches with respect to major elements compared to Ash Mountain Complex granites. (B) K_2O versus SiO_2 in AMC granitic rocks (symbols as in Fig. 4) and in the experimental melts. The gray field includes compositions of liquids with >65 wt% SiO_2 generated by partial melting of natural mafic starting compositions with K_2O contents <~1.0 wt% (Holloway and Burnham, 1972; Helz, 1976; Spulber and Rutherford, 1983; Rushmer, 1991; Beard and Lofgren, 1991; amphibolites studied by Castro et al., 2010). Ratajeski et al. (2005) conducted experiments on three Sierra Nevada batholith biotite-hornblende gabbros, which they considered to be analogs of Sierran lower crust. Castro et al. (2010) conducted melting experiments on mixtures of materials they considered analogs to subducted oceanic crust (mid-oceanic ridge basalt–derived amphibolite) and sediments (mica-rich metagraywacke, or biotite gneiss). Data shown here include melts generated from melting biotite gneiss (blue squares) and mixtures of the gneiss plus amphibolite (blue crosses).

of Sr and Y values seemingly appropriate to the starting material (cf. Table 7). We focused on experimental runs that produced partial melts that most closely resemble major element compositions of AMC granites. For example, synthetic glasses produced by Skjerlie and Johnston (1993) with silica contents >73 wt% were not included in Sr-Y models. Some experimental residual mineral modes include accessory ilmenite, titanomagnetite, apatite, spinel, corundum, rutile, kyanite, zoisite, phengite, and/or a sulfide phase. We assumed that Sr and Y are largely controlled by the major residual minerals (especially garnet, amphibole, and plagioclase) and did not include accessory phases in Sr-Y models (cf. Table 6).

Figure 20 illustrates modeled Sr and Y compositions for melts derived in experiments along with observed Sr and Y compositions for AMC LEGs. Residual mineralogies that contain garnet but no amphibole are unlikely sources for AMC LEGs (Figs. 20A, 20B). Although some melts produced in experiments conducted by Skjerlie and Patiño-Douce (2002) share broadly similar major element compositions with LEGs (Figs. 18 and 19), we did not model Sr-Y in those melts because residual mineral modes and glass percentages were not documented. Sources in the Skjerlie and Patiño-Douce (2002)

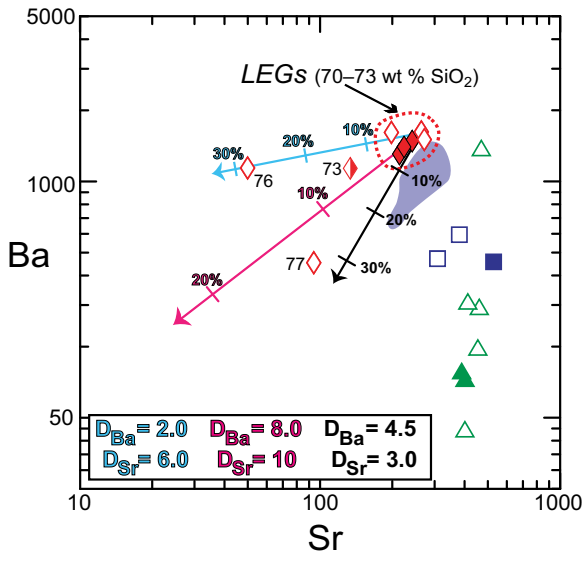

Figure 17. Log Ba (ppm) versus log Sr (ppm) for Ash Mountain Complex (AMC) intrusive rocks (symbols as in Fig. 4). Dark blue field represents data for the El Capitan Granite (Ratajeski et al., 2005). Arrows represents trends for Rayleigh fractional crystallization using bulk partition coefficients (D values) appropriate for granitic compositions. Each fractionation vector is color coded according to the D values used. Tick marks represent increments of 10% crystallization. Adjacent to symbols for AMC granites are ranges or values of wt% SiO_2. Red dashed line encompasses the least evolved granites (LEGs) of the AMC. Note the distinct trends for AMC mafic and felsic rocks.

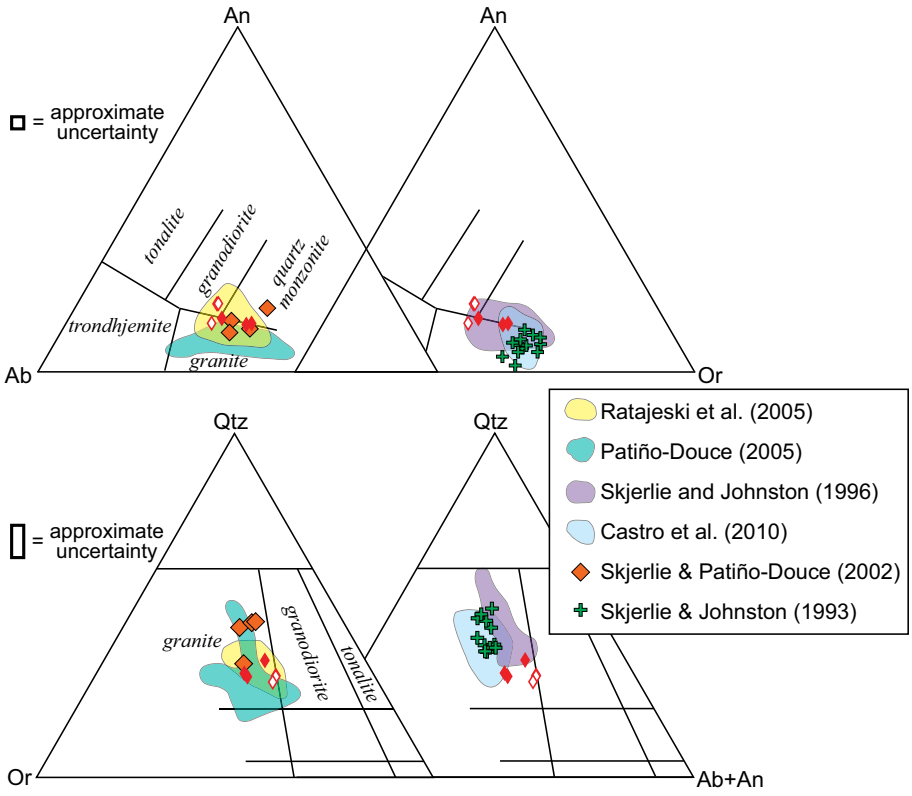

Figure 18. CIPW-normative ternary diagrams for Ash Mountain Complex (AMC) least evolved granites (LEGs; red open and filled diamonds) and granitic melts produced in experiments (see Fig. 16). Colored fields represent melt compositions from experiments (see legend). Only melts with >3.5 wt% K_2O produced in experiments by Skjerlie and Patiño-Douce (2002) are illustrated. Melt compositions from experiments documented by Skjerlie and Johnston (1993) are shown; one outlier from those experiments is not included as it might be a spurious result. Compositional fields on albite-anorthite-orthoclase (Ab-An-Or) and orthoclase-quartz-[albite+anorthite] (Or-Qtz-[Ab + An]) diagrams are after Barker (1979) and Streckeisen (1976), respectively. Uncertainties were estimated by examining variations in glass compositions generated in experiments listed in Figure 16.

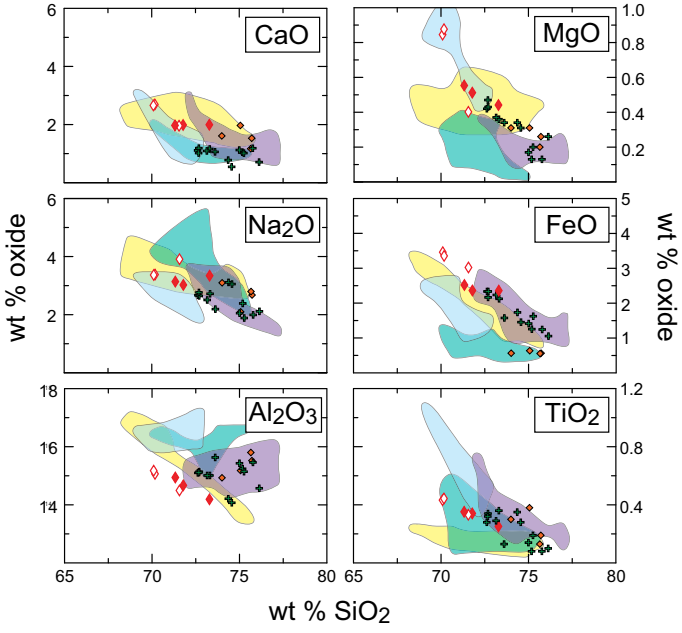

Figure 19. Silica versus major element oxides in Ash Mountain Complex (AMC) least evolved granites (LEGs) and experimentally produced melts (cf. Table 6) with SiO_2 contents >~68 wt%. Symbols and fields as in Figure 18.

experiments contain garnet, thus we assume that the derived melts would not share the low Sr/Y values characteristic of AMC LEGs.

Melts resulting from very high degrees of melting (~50%–80%; Castro et al., 2010) have Sr-Y characteristics similar to those of AMC LEGs (Fig. 20C). However, such high degrees of melting seem unlikely as melt segregation and migration appear to occur at melt fractions of ~26–40 vol% (Sawyer, 1994, and references therein) or even lower volumes (Rushmer, 1996).

Sources that contain neither garnet nor amphibole have low Sr/Y compared to AMC LEGs, although the Y contents are much higher (Fig. 20E). In order to keep Y contents low in resulting melts, it appears that amphibole, which has a K_D for Y of ~1.6 (cf. Table 4), is required in the source.

Melts produced in experiments that include amphibole but no garnet in the source (Ratajeski

TABLE 6. PARAMETERS USED IN CRUSTAL MELTING MODELS

Reference	Model name	Glass (%)	Mineral* modes normalized to 100%								Starting composition†	Range of F shown in Figures 20 and 22
			Qz	Grt	Pl	Amp	Cpx	Opx	Bt	Kfs		
Castro et al. (2010)	Cas,Gneiss, 1	40	54.5	45.5							I	30–50
	Cas,Gneiss, 2	50	55.6	11.1	33.3						I	40–60
	Cas,Gneiss, 3	82	66.7	33.3							I	70–85
	Cas,Gneiss, 4	60		64.7	35.3						I	50–70
	Mel 0.5 A	40		34.5	34.5	8.6	17.2	5.2			II	30–50
	Mel 0.5 B	50		40.0			50.0	10.0			II	40–60
	Mel 0.25	60		12.5	25.0		62.5				III	50–70
	Mel 0.75	70		66.7	16.7		16.7				IV	60–80
Ratajewski et al. (2005)	87S35a, 1591	12			51.2	46.5			2.3		V	10–30
	87S35a, 1611	12			55.3	43.5			1.2		V	10–30
	87S35a, 1602	15			54.9	45.1					V	10–30
	87S35a, 1694	12			58.3	41.7					V	10–30
	87S35a, 1619	12			61.4	38.6					V	10–30
	87S35a, 1624	10			61.9	36.9			1.2		V	10–30
	YOS-55a, 1635	22			51.3	40.8		7.9			VI	10–30
	YOS-55a, 1642	22			46.1	48.7		5.3			VI	10–30
	YOS-55a, 1644	25			45.9	41.9	5.4	6.8			VI	10–30
	YOS-55a, 1673	20	1.1		47.4	47.4	1.4	2.8			VI	10–30
	YOS-55a, 1640	20	0.3		53.3	34.2	6.8	5.5			VI	10–30
Skjerlie and Johnston (1993)	SKJ John 1	26	27.9		55.7		12.9	3.6			V, VI, VII, VIII, IX, X	20–35
	SKJ John 2	29	28.4		57.5		12.7	1.5			V, VI, VII, VIII, IX, X	20–35
	SKJ John 3	30	28.0		57.6		14.4				V, VI, VII, VIII, IX, X	20–35
Skjerlie and Johnston (1996)	S&J1	9	13.3	4.4	51.1	31.1					VII, VIII, IX, X	10–20
	S&J2	19	17.3	7.4	46.9	21.0	7.4				VII, VIII, IX, X	10–30
	S&J3	34	7.8	15.6	46.9		29.7				VII, VIII, IX, X	20–40
	S&J4	30	7.2	30.4	46.4		15.9				VII, VIII, IX, X	20–40
	S&J5	22	11.7	18.2	39.0		20.8		10.4		VII, VIII, IX, X	20–40
	S&J6	25	12.3	24.7	37.0		26.0				VII, VIII, IX, X	20–40
	S&J7	26	13.5	21.6	35.1		29.7				VII, VIII, IX, X	20–40
	S&J8	29	6.9	25.0	38.9		29.2				VII, VIII, IX, X	20–40
	S&J9	40	1.7	43.1	36.2		19.0				VII, VIII, IX, X	30–50
	S&J10	12	18.4	26.4	29.9		25.3				VII, VIII, IX, X	10–20
	S&J11	18	16.0	33.3	24.7		25.9				VII, VIII, IX, X	10–30
	S&J12	23	14.3	33.8	28.6		23.4				VII, VIII, IX, X	20–40
	S&J13	34	7.5	28.4	44.8		19.4				VII, VIII, IX, X	30–40

(*continued*)

TABLE 6. PARAMETERS USED IN CRUSTAL MELTING MODELS (*continued*)

Reference	Model name	Glass (%)	Mineral* modes normalized to 100%							Starting composition†	Range of F shown in Figures 20 and 22
			Qz	Grt	Pl	Amp	Cpx	Opx	Bt	Kfs		
Patiño-Douce (2005)	PD 1	18	13.9	22.2	33.7		11.2		2.7	16.2	VII, VIII, IX, X	10–30
	PD 2	10	21.4	19.6			24.1			35.0	VII, VIII, IX, X	5–20
	PD 3	12	17.9	23.8			24.6			33.6	VII, VIII, IX, X	5–20
	PD 4	16	15.3	26.2			25.4			33.1	VII, VIII, IX, X	5–25
	PD 5	33	14.1	31.6			24.2			30.0	VII, VIII, IX, X	20–40
	PD 6	55		45.5			28.6			25.9	VII, VIII, IX, X	40–60
	PD 7	8	32.9	18.1			33.0			15.9	VII, VIII, IX, X	5–20
	PD 8	22	22.7	22.3			39.3			15.8	VII, VIII, IX, X	15–35
	PD 9	26	18.2	24.5			40.1			17.1	VII, VIII, IX, X	15–35
	PD 10	39	13.5	32.7			40.0			13.8	VII, VIII, IX, X	30–50
	PD 11	45	19.7	41.0	17.9		21.3				VII, VIII, IX, X	35–55
	PD 12	9	27.8	15.8			45.0			11.4	VII, VIII, IX, X	5–15
	PD 13	26	21.0	19.4			52.2			7.3	VII, VIII, IX, X	15–35
	PD 14	45	12.6	27.4			58.4			1.6	VII, VIII, IX, X	35–55
	PD 15	5	46.0	17.7			36.3				VII, VIII, IX, X	5–15§
	PD 16	31	27.1	25.5			47.3				VII, VIII, IX, X	20–40§
	PD 17	50	13.5	32.6			53.9				VII, VIII, IX, X	40–60

Note: The starting compositions I–X represent various crustal sources used in partial melting models involving trace elements (Sr and Y). F—percentage of melt.
*Mineral symbols after Whitney and Evans (2010).
†Table 7 gives references for the source compositions.
§This range plots off scale in Figure 20.

et al., 2005; cf. Fig. 20D) provide the best fit for AMC LEGs. Ratajeski et al. (2005) and Sisson et al. (2005) conducted experiments on biotite-hornblende gabbros from the central SNB, which they considered to be reasonable analogs of Sierran lower crust. Ratajeski et al. (2005) found that melts from these sources have major element compositions similar to those of the El Capitan Granite in the central part of the SNB. Ratajeski et al. (2005) calculated trace element abundances (REEs, Rb, Ba, Sr, Th, U) in partial melts produced in their experiments using trace element concentrations in the starting compositions, run-product modal data, and published partition coefficients (or other predictive expressions); they found good matches between their calculated trace element abundances and the observed abundances in the El Capitan Granite (Fig. 21). Both major and trace element compositions of AMC LEGs are remarkably similar to those of the El Capitan Granite (Figs. 7 and 21). Using parameters given in Table 6 for experimental melts of Ratajeski et al. (2005) and Sr and Y abundances for one of their starting materials (Table 7), modeled Sr and Y abundances are close fits to AMC LEGs (Fig. 19D). Excellent matches are achieved (Fig. 22) when somewhat lower Sr (250–300 ppm) contents are used in the models. These Sr abundances are similar to estimates for lower to middle continental crust (see the EarthRef.org Geochemical Earth Reference Model database: http://earthref.org/GERM).

The majority of apparent Ti-in-zircon temperatures calculated for AMC granites range from ~625 to ~775 °C (cf. Fig. 6). Among the partial melt experiments examined here (Fig. 16), those of Ratajeski et al. (2005) involve the lowest range in temperatures (825–850 °C), which is ~50–225 °C higher than calculated zircon temperatures. Other experiments examined here (Fig. 16) involve higher temperatures, ranging from 875 to 1150 °C. Although calculated zircon temperatures may be lower than actual crystallization (and magmatic) temperatures (Fu et al., 2008), we believe that the Ratajeski et al. (2005) experiments are the best analogues, assuming that crustal anatexis was the dominant process responsible in generating AMC LEGs.

In summary, if AMC felsic magmas are the result of crustal anatexis, the most plausible sources are amphibole-bearing assemblages that underwent moderate (10%–30%) degrees of melting at temperatures <850 °C. Sr-Y models indicate that garnet was not a residual phase in the source, thus restricting melting to depths <~30 km (cf. Fig. 2 in Saleeby et al., 2003, and references therein). Although AMC sources might have had lower Sr and Y contents than SNB gabbros considered to be analogs of

TABLE 7. Sr AND Y CONTENTS USED IN CRUSTAL MELTING MODELS

Starting composition	Source	Sr (ppm)	Y (ppm)
I	Castro et al. (2010), Table 1 therein, Bt-gneiss	131.8	33.1
II	Castro et al. (2010), Table 1 therein, Mél 2	170.1	28.3
III	Castro et al. (2010), Table 1 therein, Mél 1	189.3	26
IV	Castro et al. (2010), Table 1 therein, Mél 3	151	30.7
V	Sisson et al. (1996), Table 1 therein, sample 87S35a	850	22
VI	Ratajeski et al. (2001), Table 2 therein, sample YOS-55a	457	18
VII	Hoffman et al. (2011), Supplementary Data 2; tonalite, 468001	227	9.64
VIII	Lackey et al. (2012), Table 2 therein; representative range of Bass Lake Tonalite (Blt) compositions	367	10
IX		428	25
X		630	18

Note: The starting compositions I–X represent various crustal sources used in partial melting models involving trace elements (Sr and Y) illustrated in Figures 20 and 22.

Sierran lower crust (Ratajeski et al., 2005; Sisson et al., 2005), they otherwise share similar major element and other trace element characteristics.

Transition ca. 105 Ma

The increasing crustal input to AMC magmas after 105 Ma appears to coincide with a time when the Sierran arc was undergoing a significant increase in magmatic activity, as recorded by distributions of U-Pb zircon age and pluton area (Lackey et al., 2008). This period also corresponds to an apparent increase in the volume or preservation of 105–102 Ma rhyolites and dacites in pendants and septa at Ash Peaks, Redwood Mountain, and Boyden Cave in the Sequoia–Kings Canyon region (Moore and Sisson, 1987; Saleeby et al., 1990), the Erskine Canyon sequence in the southern Sierra (Busby-Spera and Saleeby, 1990), and in the Ritter Range area with eruption of 102–108 ± 3 Ma rhyolites (Memeti et al., 2010b). The 105–102 Ma rhyolites from the Sequoia region and in the southern Sierra have high-$\delta^{18}O$ zircons (>7‰; Lackey et al. 2005, 2008), consistent with crustal melt sources.

The 105–102 Ma interval appears to record major changes in deformation in the Sierra, in addition to the increasing magmatic activity. In particular, the proposed transbatholith Mojave–Snow Lake fault appears to have deactivated ca. 102 Ma or earlier (Memeti et al., 2010b). The initial activation of the proto–Kern Canyon fault system appears to be showing initial stages of strike-slip movement with a "cryptic deformational phase" (Nadin and Saleeby, 2008, p. 21) occurring in the 105–102 Ma Erskine Canyon sequence (Busby-Spera and Saleeby, 1990; Saleeby et al., 2008). Thus, this period appears to record major redistribution of faulting in the batholith. Such a change in deformation style aligns with the proposal by Matthews et al. (2012) that a major global tectonic reorganization occurred between 105 and 100 Ma.

We hypothesize that the magmatic and deformational changes during this period are linked in the SNB and that, within the AMC, the transition from stage 1 to stage 2 and stage 3 records a tectonically induced shift in magmatic source. The greater crustal participation in the production of stage 2 and 3 magmas is possibly related to increased melting of existing crust or melting of crust at higher levels in the arc. This shift may record insertion of fertile crust into source regions by underthrusting (e.g., Ducea and Barton, 2007). Whereas a 25–50-m.y.-cycle of

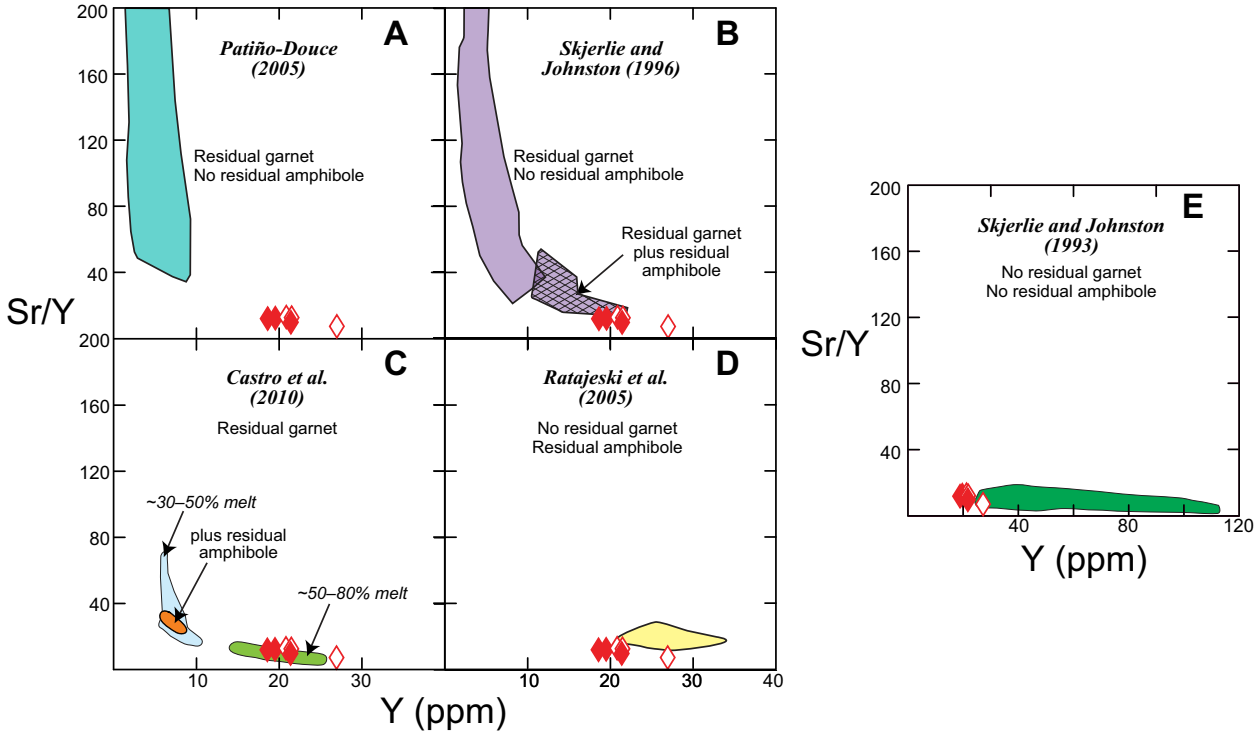

Figure 20. Sr/Y versus Y (ppm) contents in Ash Mountain Complex least evolved granites (LEGs; red open and filled diamonds). Each panel shows calculated Sr-Y compositions for partial melts produced in experiments (cf. Fig. 16). Table 6 provides details of the parameters (residual mineral assemblages, degree of melting) assumed in the model calculations. Table 7 gives Sr and Y contents assumed for initial starting compositions. Each panel indicates the residual mineralogy. Note the change in scale for Y contents in E.

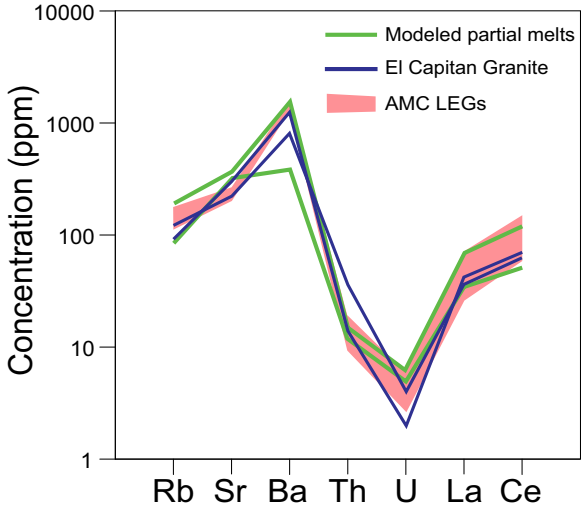

Figure 21. Calculated trace element abundances in partial melts produced in an experiment (run 1694) using Sierra Nevada batholith mafic source rock (green lines; see Fig. 6 and Table 5 in Ratajeski et al., 2005). Also shown are observed trace element abundances in two samples of the El Capitan Granite (blue lines) and Ash Mountain Complex (AMC) least evolved granites (LEGs) (pink shaded field).

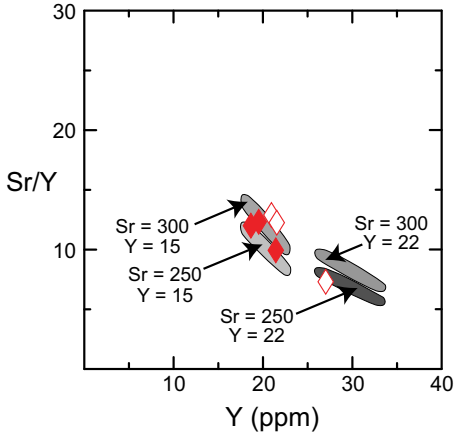

Figure 22. Sr/Y versus Y (ppm) contents in Ash Mountain Complex (AMC) least evolved granites (LEGs; red open and filled diamonds). Also shown are calculated Sr/Y and Y for synthetic melts using modes and F values from Ratajeski et al. (2005), given in Table 6. Initial Sr and Y values were assumed: Sr = 250, 300; Y = 15, 22. The resulting melts are illustrated by shaded fields, and the Sr and Y used in the models are indicated.

magmatic reinvigoration is proposed to explain the magmatic flare-ups in the Triassic, Jurassic, and Cretaceous (DeCelles et al., 2009), we suggest that similar recharge of magma sources by crustal additions from the forearc or retroarc may have operated on shorter time scales. We recognize that our isotopic and age-dating sampling is limited, and emphasize that these ideas should be tested further.

CONCLUSIONS

Based on field relationships and zircon U-Pb analyses of rocks within the AMC, we propose that the complex formed in three stages of intrusion dominated by mafic and felsic compositions. Stage 1 magmatism occurred ca. 105 Ma and consisted of two gabbros, a gabbro/gabbrodiorite, and a granite. Stages 2 and 3 magmatism occurred ca. 104 Ma and ca. 103 Ma, respectively, and consisted of granites. Calculated Ti-in-zircon temperatures and Hf fractionation data support a model where contact between cooler granitic magmas likely caused relatively rapid cooling of hotter mafic magmas, preventing significant fractionation of the mafic magmas, while granitic magmas cooled more slowly, permitting more fractionation.

Major and trace element data from the AMC are broadly similar to those of other studies of the SNB, suggesting that the AMC is an excellent locality to examine the petrogenesis of coeval mafic and felsic magmas. Our trace element models of crystal fractionation, with or without assimilation, are consistent with trace element variations among AMC gabbros and gabbrodiorite. However, fractionation models cannot account for the high concentrations or wide ranges of incompatible trace element concentrations in AMC felsic rocks (Figs. 12–14). Crustal anatexis of an amphibole-bearing, mafic crustal source appears to best explain the observed major and trace element and isotopic compositions of AMC granitic rocks. Among the partial melting experiments considered here (Fig. 16), the experimentally synthesized glasses of Ratajeski et al. (2005), derived by melting of biotite-hornblende gabbros, best fit the measured major element compositions of AMC felsic rocks (Figs. 18 and 19). The temperatures of the Ratajeski et al. (2005) experiments (825–850 °C) are the closest fits to the majority of apparent Ti-in-zircon temperatures calculated for AMC granites (~625–775 °C). The pressure used in these experiments (7 kbar) results in an amphibolitic, garnet-free residual source mineralogy. Modeled Sr-Y variations in liquids derived from this source mineralogy are similar to those observed in AMC LEGs. We thus hypothesize that crustal anatexis took place at depths <~30 km.

If AMC granites were derived by melting of mantle-derived mafic crust, they should exhibit mantle-like isotopic characteristics. We suggest that the low variability in isotopic compositions of stage 1 gabbros and granites [$^{87}Sr/^{86}Sr_{(i)}$ = 0.7051–0.7059; $\varepsilon_{Nd(i)}$ = –3.1 to –2.1] supports this hypothesis. The more evolved isotopic compositions of the younger stage 2 and 3 granites [$^{87}Sr/^{86}Sr_{(i)}$ = 0.7064–0.7083; $\varepsilon_{Nd(i)}$ = –6.1 to –3.7] indicate a larger input from evolved crust (Fig. 15). The AMC rocks thus appear to capture a temporal transition between the ca. 105 Ma emplacement of stage 1 rocks [$^{87}Sr/^{86}Sr_{(i)}$ < 0.7060] with more juvenile sources and the post–105 Ma emplacement of stage 2 and 3 rocks [$^{87}Sr/^{86}Sr_{(i)}$ > 0.7060] with greater involvement of older continental crust.

The AMC provides an example of coeval mafic and felsic magmatism involving different sources at different levels within the lithosphere. The brief timing and change of isotopic compositions of stage 1 relative to stage 2 and 3 units suggest that these magmas might represent a transition in sources beneath the SNB, from a more primitive mantle source to a source region involving a greater crustal component, potentially related to intra-arc compression (e.g., Ducea and Barton, 2007). We suggest that the compositional diversity of the AMC can be produced through partial melting of crustal and mantle sources, with fractionation and assimilation playing relatively minor roles. We also suggest that mafic and felsic compositions of the AMC could represent end members of mixing processes, which may have generated the intermediate magmas that dominate much of the SNB.

ACKNOWLEDGMENTS

We benefitted from reviews by Alan D. Chapman and an anonymous reviewer and editorial handling by Cathy Busby and Carol Frost. We thank fellow Keck student researchers Mary Badame, Megan D'Errico, Stanley Hensley, Jesslyn Starnes, and Julianne Wallan for camaraderie and interesting discussions, and research advisors Steve Wojtal and Erik Klemetti for their support in the field. We also thank Joe Wooden and Brad Ito at the U.S. Geological Survey–Stanford University (Stanford, California) SHRIMP Lab for working with us and sharing their knowledge of zircon analyses, and the rangers and staff of Sequoia National Park for their role in making our field

work possible. This research was funded by Keck Geology Consortium (National Science Foundation [NSF] Research Experiences for Undergraduates 1005122), Trinity University (San Antonio, Texas) Department of Geosciences, and an Exxon-Mobile Enhanced Grant. Additional support came from NSF grant EAR-0948706 to Lackey; the Pomona College (Claremont, California) XRF Laboratory was initiated with funding from NSF grant DUE-0942447 and Pomona College.

REFERENCES CITED

Ague, J.J., and Brimhall, G.H., 1988, Regional variations in bulk chemistry, mineralogy, and the compositions of mafic and accessory minerals in the batholiths of California: Geological Society of America Bulletin, v. 100, p. 891–911, doi:10.1130/0016-7606(1988)100<0891:RVIBCM>2.3.CO;2.

Annen, C., Blundy, J.D., and Sparks, R.S.J., 2006, The genesis of intermediate and silicic magmas in deep crustal hot zones: Journal of Petrology, v. 47, p. 505–539, doi:10.1093/petrology/egi084.

Arth, J.G., 1976, Behaviour of trace elements during magmatic processes—A summary of theoretical models and their applications: U.S. Geological Survey Journal of Research, v. 4, p. 41–47.

Barbarin, B., 1990, Plagioclase xenocrysts and mafic magma enclaves in some granitoids of the Sierra Nevada batholith, California: Journal of Geophysical Research, v. 95, no. B11, p. 17747–17756, doi:10.1029/JB095iB11p17747.

Barbarin, B., 1991, Enclaves of the Mesozoic calc-alkaline granitoids of the Sierra Nevada Batholith, California, *in* Didier, J., and Barbarin, B., eds., Enclaves and granite petrology: Developments in Petrology 13: Amsterdam, Elsevier, p. 135–153.

Barker, F., 1979, Trondhjemite: Definition, environment and hypotheses of origin, *in* Barker, F., ed., Trondhjemites, dacites and related rocks: Elsevier, Amsterdam, p. 1–12.

Barth, A.P., and Wooden, J.L., 2010, Coupled elemental and isotopic analyses of polygenetic zircons from granitic rocks by ion microprobe, with implications for melt evolutions and the sources of granitic magmas: Chemical Geology, v. 277, p. 149–159, doi:10.1016/j.chemgeo.2010.07.017.

Bateman, P.C., 1992, Plutonism in the central part of Sierra Nevada Batholith, California: U.S. Geological Survey Professional Paper 1483, 186 p.

Bateman, P.C., and Chappell, B.W., 1979, Crystallization, fractionation, and solidification of the Tuolumne Intrusive Series, Yosemite National Park, California: Geological Society of America Bulletin, v. 90, p. 465–482, doi:10.1130/0016-7606(1979)90<465:CFASOT>2.0.CO;2.

Beard, B.L., and Glazner, A.F., 1995, Trace element and Sr and Nd isotopic composition of mantle xenoliths from the Big Pine volcanic field, California: Journal of Geophysical Research, v. 100, no. B3, p. 4169–4179, doi:10.1029/94JB02883.

Beard, J.S., and Lofgren, G.E., 1991, Dehydration melting and water-saturated melting of basaltic and andesitic greenstones and amphibolites at 1.3, and 6.9 kb: Journal of Petrology, v. 32, p. 365–401, doi:10.1093/petrology/32.2.365.

Bergantz, G.W., 1989, Underplating and partial melting: Implications for melt generation and extraction: Science, v. 245, p. 1093–1095, doi:10.1126/science.245.4922.1093.

Black, L.P., Kamo, S.L., Allen, C.M., Davis, D.W., Aleinikoff, J.N., Valley, J.W., Mundil, R., Campbell, I.H., Korsch, R.J., Williams, I.S., and Foudoulis, C., 2004, Improved $^{207}Pb/^{238}U$ microprobe geochronology by the monitoring of a trace-element-related matrix effect: SHRIMP, ID-TIMS, ELA-ICP-MS and oxygen isotope documentation for a series of zircon standards: Chemical Geology, v. 205, p. 115–140, doi:10.1016/j.chemgeo.2004.01.003.

Bowen, N.L., 1928, The evolution of the igneous rocks: Princeton, New Jersey, Princeton University Press, 332 p.

Brophy, J.G., 1991, Composition gaps, critical crystallinity, and fractional crystallization in orogenic (calc-alkaline) magmatic systems: Contributions to Mineralogy and Petrology, v. 109, p. 173–182, doi:10.1007/BF00306477.

Busby-Spera, C.J., and Saleeby, J.B., 1990, Intra-arc strike-slip fault exposed at batholithic levels in the southern Sierra Nevada, California: Geology, v. 18, p. 255–259, doi:10.1130/0091-7613(1990)018<0255:IASSFE>2.3.CO;2.

Castro, A., Gerya, T., García-Casco, A., Fernández, C., Díaz-Alvarado, J., Moreno-Ventas, I., and Löw, I., 2010, Melting relations of MORB-sediment mélanges in underplated mantle wedge plumes; Implications for the origin of Cordilleran-type batholiths: Journal of Petrology, v. 51, p. 1267–1295, doi:10.1093/petrology/egq019.

Chen, J.H., and Moore, J.G., 1982, Uranium-lead isotopic ages from the Sierra Nevada batholith, California: Journal of Geophysical Research, v. 87, no. B6, p. 4761–4784, doi:10.1029/JB087iB06p04761.

Chen, J.H., and Tilton, G.R., 1991, Applications of lead and strontium isotopic relationships to the petrogenesis of granitoid rocks, central Sierra Nevada batholith, California: Geological Society of America Bulletin, v. 103, p. 439–447, doi:10.1130/0016-7606(1991)103<0439:AOLASI>2.3.CO;2.

Claiborne, L.L., Miller, C.F., and Wooden, J.L., 2010, Trace element composition of igneous zircon: A thermal and compositional record of the accumulation and evolution of a large silicic batholith, Spirit Mountain, Nevada: Contributions to Mineralogy and Petrology, v. 160, p. 511–531, doi:10.1007/s00410-010-0491-5.

Clemens-Knott, D., 1992, Geologic and isotopic investigations of the Early Cretaceous Sierra Nevada batholith, Tulare County, California, and the Ivrea Zone, northwest Italian Alps: Examples of interaction between mantle-derived magma and continental crust [Ph.D. thesis]: Pasadena, California Institute of Technology, 359 p.

Coleman, D.S., and Glazner, A.F., 1997, The Sierra crest magmatic event: Rapid formation of juvenile crust during the Late Cretaceous in California: International Geology Review, v. 39, p. 768–787, doi:10.1080/00206819709465302.

Coleman, D.S., Frost, T.P., and Glazner, A.F., 1992, Evidence from the Lamarck Granodiorite for rapid Late Cretaceous crust formation in California: Science, v. 258, p. 1924–1926, doi:10.1126/science.258.5090.1924.

Coleman, D.S., Glazner, A.F., Miller, J.S., Bradford, K.J., Frost, T.P., Joye, J.L., and Bachl, C.A., 1995, Exposure of a Late Cretaceous layered mafic-felsic magma system in the central Sierra Nevada batholith, California: Contributions to Mineralogy and Petrology, v. 120, p. 129–136, doi:10.1007/BF00287110.

Coleman, D.S., Gray, W., and Glazner, A.F., 2004, Rethinking the emplacement and evolution of zoned plutons: Geochronologic evidence for incremental assembly of the Tuolumne Intrusive Suite, California: Geology, v. 32, p. 433–436, doi:10.1130/G20220.1.

Cox, K.G., Bell, J.D., and Pankhurst, R.J., 1979, The interpretation of igneous rocks: London, George, Allen and Unwin, 450 p.

Davis, J.W., Coleman, D.S., Gracely, J.T., Gaschnig, R., and Stearns, M., 2012, Magma accumulation rates and thermal histories of plutons of the Sierra Nevada batholith, CA: Contributions to Mineralogy and Petrology, v. 163, p. 449–465, doi:10.1007/s00410-011-0683-7.

DeCelles, P.G., Ducea, M.N., Kapp, P., and Zandt, G., 2009, Cyclicity in Cordilleran orogenic systems: Nature Geoscience, v. 2, p. 251–257, doi:10.1038/ngeo469.

DePaolo, D.J., 1980, Sources of continental crust: Neodymium isotope evidence from the Sierra Nevada and Peninsular ranges: Science, v. 209, p. 684–687, doi:10.1126/science.209.4457.684.

DePaolo, D.J., 1981, A neodymium and strontium isotopic study of Mesozoic calcalkaline granitic batholiths of the Sierra Nevada and Peninsular Ranges, California: Journal of Geophysical Research, v. 86, no. B11, p. 10470–10488, doi:10.1029/JB086iB11p10470.

Dickinson, W.R., 1981, Plate tectonics and the continental margin of California, *in* Ernst, W.G., ed., The geotectonic development of California: Rubey Volume 1: Englewood Cliffs, New Jersey, Prentice-Hall, p. 1–28.

Dodge, F.C.W., Calk, L.C., and Kistler, R.W., 1986, Lower crustal xenoliths, Chinese Peak lava flow: Journal of Petrology, v. 27, p. 1277–1304, doi:10.1093/petrology/27.6.1277.

Dodge, F.C.W., Lockwood, J.P., and Calk, L.C., 1988, Fragments of the mantle and crust from beneath the Sierra Nevada Batholith: Xenoliths in a volcanic pipe near Big Creek, California: Geological Society of America Bulletin, v. 100, p. 938–947, doi:10.1130/0016-7606(1988)100<0938:FOTMAC>2.3.CO;2.

Dorais, M.J., Whitney, J.A., and Roden, M.F., 1990, Origin of mafic enclaves in the Dinkey Creek Pluton, central Sierra Nevada Batholith, California: Journal of Petrology, v. 31, p. 853–881, doi:10.1093/petrology/31.4.853.

Drummond, M.S., and Defant, M.J., 1990, A model for trondhjemite-tonalite-dacite genesis and crustal growth via slab melting: Archean to modern comparisons: Journal of Geophysical Research, v. 95, no. B13, p. 21503–21521, doi:10.1029/JB095iB13p21503.

Ducea, M., 2001, The California arc: Thick granitic batholiths, eclogitic residues, lithospheric-scale thrusting, and magmatic flare-ups: GSA Today, v. 11, p. 4–10, doi:10.1130/1052-5173(2001)011<0004:TCATGB>2.0.CO;2.

Ducea, M., 2002, Constraints on the bulk composition and root foundering rates of continental arcs: A California arc perspective: Journal of Geophysical Research, v. 107, no. B11, p. ECV 15-1–ECV 15-13, doi:10.1029/2001JB000643.

Ducea, M.N., and Barton, M.D., 2007, Igniting flare-up events in Cordilleran arcs: Geology, v. 35, p. 1047–1050, doi:10.1130/G23898A.1.

Dufek, J., and Bachmann, O., 2010, Quantum magmatism: Magmatic compositional gaps generated by melt-crystal dynamics: Geology, v. 38, p. 687–690, doi:10.1130/G30831.1.

Dufek, J., and Bergantz, G.W., 2005, Lower crustal magma genesis and preservation: A stochastic framework for the evaluation of basalt-crust interaction: Journal of Petrology, v. 46, p. 2167–2195, doi:10.1093/petrology/egi049.

Ferriss, E.D.A., Essene, E.J., and Becker, U., 2008, Computational study of the effect of pressure on the Ti-in-zircon geothermometer: European Journal of Mineralogy, v. 20, p. 745–755, doi:10.1127/0935-1221/2008/0020-1860.

Ferry, J.M., and Watson, E.B., 2007, New thermodynamic models and revised calibrations for the Ti-in-zircon and Zr-in-rutile thermometers: Contributions to Mineralogy and Petrology, v. 154, p. 429–437, doi:10.1007/s00410-007-0201-0.

Frost, T.P., and Mahood, G.A., 1987, Field, chemical, and physical constraints on mafic-felsic magma interaction in the Lamarck Granodiorite, Sierra Nevada, California: Geological Society of America Bulletin, v. 99, p. 272–291, doi:10.1130/0016-7606(1987)99<272:FCAPCO>2.0.CO;2.

Fu, B., Page, F.Z., Cavosie, A.J., Fournelle, J., Kita, N.T., Lackey, J.S., Wilde, S.A., and Valley, J.W., 2008, Ti-in-zircon thermometry: applications and limitations: Contributions to Mineralogy and Petrology, v. 156, p. 197–215, doi:10.1007/s00410-008-0281-5.

Giletti, B., 1986, Diffusion effects on oxygen isotope temperatures of slowly cooled igneous and metamorphic rocks: Earth and Planetary Science Letters, v. 77, p. 218–228, doi:10.1016/0012-821X(86)90162-7.

Giletti, B., 1991, Rb and Sr diffusion in alkali feldspars, with implications for cooling histories of rocks: Geochimica et Cosmochimica Acta, v. 55, p. 1331–1343, doi:10.1016/0016-7037(91)90311-R.

Hamelin, B., Manhes, G., Albarede, F., and Allegre, C.J., 1985, Precise lead isotope measurements by the double spike technique: A reconsideration: Geochimica et Cosmochimica Acta, v. 49, p. 173–182, doi:10.1016/0016-7037(85)90202-9.

Hart, S.R., 1984, A large scale isotope anomaly in the Southern Hemisphere mantle: Nature, v. 309, p. 753–757, doi:10.1038/309753a0.

Hayden, L.A., and Watson, E.B., 2007, Rutile saturation in hydrous siliceous melts and its bearing on Ti-thermometry of quartz and zircon: Earth and Planetary Science Letters, v. 258, p. 561–568, doi:10.1016/j.epsl.2007.04.020.

Helz, R.T., 1976, Phase relations of basalts in their melting ranges at P_{H2O} = 5 kb. Part II. Melt compositions: Journal of Petrology, v. 17, p. 139–193, doi:10.1093/petrology/17.2.139.

Hensley, S.A., Loewy, S.L., Lackey, J.S., and Wooden, J.L., 2010, Temporal variation in pluton-wallrock interaction in the Sierran Arc: Geological Society of America Abstracts with Programs, v. 42, no. 5, p. 627.

Hildreth, W., 1981, Gradients in silicic magma chambers: Implications for lithospheric magmatism: Journal of Geophysical Research, v. 86, no. B11, p. 10153–10192, doi:10.1029/JB086iB11p10153.

Hildreth, W., and Moorbath, S., 1988, Crustal contributions to arc magmatism in the Andes of central Chile: Contributions to Mineralogy and Petrology, v. 98, p. 455–489, doi:10.1007/BF00372365.

Hoffmann, J.E., Münker, C., Næraa, T., Rosing, M.T., Herwartz, D., Garbe-Schönberg, D., and Svahnberg, H., 2011, Mechanisms of Archean crust formation inferred from high-precision HFSE systematics in TTGs: Geochimica et Cosmochimica Acta, v. 75, p. 4157–4178, doi:10.1016/j.gca.2011.04.027.

Holland, J., Surpless, B., Lackey, J.S., Loewy, S.L., and Wooden, J.L., 2010, Intrusive history of the Ash Mountain Complex, Sequoia National Park: Geological Society of America Abstracts with Programs, v. 42, no. 5, p. 627.

Holloway, J.R., and Burnham, C.W., 1972, Melting relations of basalt with equilibrium water pressure less than total pressure: Journal of Petrology, v. 13, p. 1–29, doi:10.1093/petrology/13.1.1.

Ireland, T.R., and Williams, I.S., 2003, Considerations in zircon geochronology by SIMS, *in* Hanchar, J.M., and Hoskin, P.W.O., eds., Zircon: Mineralogical Society of America Reviews in Mineralogy and Geochemistry 53, p. 215–241, doi:10.2113/0530215.

Johnson, K., Barnes, C.G., and Miller, C.A., 1997, Petrology, geochemistry, and genesis of high-Al tonalite and trondhjemites of the Cornucopia Stock, Blue Mountains, northeastern Oregon: Journal of Petrology, v. 38, p. 1585–1611, doi:10.1093/petroj/38.11.1585.

Kistler, R.W., 1990, Two different lithosphere types in the Sierra Nevada, California, *in* Anderson, J.L., ed., The nature and origin of Cordilleran magmatism: Geological Society of America Memoir 174, p. 271–281.

Kistler, R.W., and Fleck, R.J., 1994, Field guide for a transect of the central Sierra Nevada, California: Geochronology and isotope geology: U.S. Geological Survey Open-File Report 94-0267, 50 p.

Kistler, R.W., and Peterman, Z.E., 1973, Variations in Sr, Rb, K, Na, and initial $^{87}Sr/^{86}Sr$ in Mesozoic granitic rocks and intruded wall rocks in central California: Geological Society of America Bulletin, v. 84, p. 3489–3512, doi:10.1130/0016-7606(1973)84<3489:VISRKN>2.0.CO;2.

Kistler, R.W., and Peterman, Z.E., 1978, Reconstruction of crustal blocks of California on the basis of initial strontium isotopic compositions of Mesozoic granitic rocks: U.S. Geological Survey Professional Paper 1071, p. 16–17, doi:10.1130/0016-7606(1973)84<3489:VISRKN>2.0.CO;2.

Kistler, R.W., Chappell, B.W., Peck, D.L., and Bateman, P.C., 1986, Isotopic variation in the Tuolumne Intrusive Suite, central Sierra Nevada, California: Contributions to Mineralogy and Petrology, v. 94, p. 205–220, doi:10.1007/BF00592937.

Lackey, J.S., Valley, J.W., and Saleeby, J.B., 2005, Supracrustal input to magmas in the deep crust of Sierra Nevada batholith: Evidence from high-$\delta^{18}O$ zircon: Earth and Planetary Science Letters, v. 235, p. 315–330.

Lackey, J.S., Valley, J.W., and Hinke, H.J., 2006, Deciphering the source and contamination history of peraluminous magmas using ^{18}O of accessory minerals: Examples from garnet-bearing plutons of the Sierra Nevada batholith: Contributions to Mineralogy and Petrology, v. 151, p. 20–44, doi:10.1007/s00410-005-0043-6.

Lackey, J.S., Valley, J.W., Chen, J.H., and Stockli, D.F., 2008, Dynamic magma systems, crustal recycling, and alteration in the central Sierra Nevada batholiths: The oxygen isotope record: Journal of Petrology, v. 49, p. 1397–1426, doi:10.1093/petrology/egn030.

Lackey, J.S., Cecil, M.R., Windham, C.J., Frazer, R.E., Bindeman, I.N., and Gehrels, G.E., 2012, The Fine Gold intrusive suite: The roles of basement terranes and magma source development in the Early Cretaceous Sierra Nevada batholith: Geosphere, v. 8, p. 292–313, doi:10.1130/GES00745.1.

Lee, C.-T., Yin, Q., Rudnick, R.L., Chesley, J.T., and Jacobsen, S.B., 2000, Osmium isotopic evidence for Mesozoic removal of lithospheric mantle beneath the Sierra Nevada, California: Science, v. 289, p. 1912–1916, doi:10.1126/science.289.5486.1912.

Lee, C.-T., Cheng, X., and Horodyskyj, U., 2006, The development and refinement of continental arcs by primary basaltic magmatism, garnet pyroxenite accumulation, basaltic recharge and delamination: Insights from the Sierra Nevada: Contributions to Mineralogy and Petrology, v. 151, p. 222–242, doi:10.1007/s00410-005-0056-1.

Lee, C.-T., Morton, D.M., Kistler, R.W., and Baird, A.K., 2007, Petrology and tectonics of Phanerozoic continent formation: From island arcs to accretion and continental arc magmatism: Earth and Planetary Science Letters, v. 263, p. 370–387, doi:10.1016/j.epsl.2007.09.025.

Ludwig, K.R., 2000, Isoplot/Ex2.45, a geochronological tool kit for Microsoft Excel: Berkeley, California, Berkeley Geochronological Center Special Publication 1a, 55 p.

Martin, H., 1987, Petrogenesis of Archaean trondhjemites, tonalities, and granodiorites from eastern Finland: Major and trace element geochemistry: Journal of Petrology, v. 28, p. 921–953, doi:10.1093/petrology/28.5.921.

Martin, M.W., and Walker, J.D., 1992, Extending the western North American Proterozoic and Paleozoic continental crust through the Mojave Desert: Geology, v. 20, p. 753–756, doi:10.1130/0091-7613(1992)020<0753:ETWNAP>2.3.CO;2.

Matthews, K.J., Seton, M., and Muller, R.D., 2012, A global-scale plate reorganization event at 105–100 Ma: Earth and Planetary Science Letters, v. 355-56, p. 283–298, doi:10.1016/j.epsl.2012.08.023.

Mazdab, F.K., and Wooden, J.L., 2006, Trace element analysis in zircon by ion microprobe (SHRIMP-RG): Technique and applications: Geochimica et Cosmochimica Acta, v. 70, supplement 1, p. A405, doi:10.1016/j.gca.2006.06.817.

Memeti, V., Paterson, S., Matzel, J., Mundil, R., and Okaya, D., 2010a, Magmatic lobes as "snapshots" of magma chamber growth and evolution in large, composite batholiths: An example from the Tuolumne intrusion, Sierra Nevada, California: Geological Society of America Bulletin, v. 122, p. 1912–1931, doi:10.1130/B30004.1.

Memeti, V., Gehrels, G.E., Paterson, S.R., Thompson, J.M., Mueller, R.M., and Pignotta, G.S., 2010b, Evaluating the Mojave-Snow Lake fault hypothesis and origins of central Sierran metasedimentary pendant strata using detrital zircon provenance analyses: Lithosphere, v. 2, p. 341–360, doi:10.1130/L58.1.

Menzies, M.A., Leeman, W.P., and Hawkesworth, C.J., 1983, Isotope geochemistry of Cenozoic volcanic rocks reveals mantle heterogeneity below western USA: Nature, v. 303, p. 205–209, doi:10.1038/303205a0.

Miller, J.S., Glazner, A.F., Farmer, G.L., Suayah, I.B., and Keith, L.A., 2000, A Sr, Nd and Pb isotopic study of mantle domains and crustal structure from Miocene volcanic rocks of the Mojave Desert, California: Geological Society of America Bulletin, v. 112, p. 1264–1279, doi:10.1130/0016-7606(2000)112<1264:ASNAPI>2.0.CO;2.

Mills, R.D., Glazner, A.F., and Coleman, D.S., 2009, Scale of pluton/wall rock interaction near May Lake, Yosemite National Park, CA, USA: Contributions to Mineralogy and Petrology, v. 158, p. 263–281, doi:10.1007/s00410-009-0381-x.

Moore, J.G., 2001, Exploring the Highest Sierra: Palo Alto, California, Stanford University Press, 427 p.

Moore, J.G., and Sisson, T.W., 1987, Geologic map of the Triple Divide Peak quadrangle, Tulare County, California: U.S. Geological Survey Geologic Quadrangle Map GQ-1636, scale: 1:62,500.

Mukhopadhyay, B., and Manton, W.I., 1994, Upper-mantle fragments from beneath the Sierra Nevada Batholith: Partial fusion, fractional crystallization, and metasomatism in a subduction-related ancient lithosphere: Journal of Petrology, v. 35, p. 1417–1450, doi:10.1093/petrology/35.5.1417.

Nadin, E.S., and Saleeby, J.B., 2008, Disruption of regional primary structure of the Sierra Nevada batholith by the Kern Canyon fault system, California, *in* Wright, J.E., and Shervais, J.W., eds., Ophiolites, arcs, and batholiths: A tribute to Cliff Hopson: Geological Society of America Special Paper 438, p. 429–454, doi:10.1130/2008.2438(15).

Nelson, W.R., Dorais, M.J., Christiansen, E.H., and Hart, G.L., 2013, Petrogenesis of Sierra Nevada plutons inferred from the Sr, Nd, and O isotopic signatures of mafic igneous complexes in Yosemite Valley, California: Contributions to Mineralogy and Petrology, v. 165, p. 397–417.

Patiño-Douce, A.E., 1997, Generation of metaluminous A-type granites by low-pressure melting of calc-alkaline granitoids: Geology, v. 25, p. 743–746, doi:10.1130/0091-7613(1997)025<0743:GOMATG>2.3.CO;2.

Patiño-Douce, A.E., 2005, Vapor-absent melting of tonalite at 15–32 kbar: Journal of Petrology, v. 46, p. 275–290, doi:10.1093/petrology/egh071.

Petford, N., and Gallagher, K., 2001, Partial melting of mafic (amphibolitic) lower crust by periodic influx of basaltic magma: Earth and Planetary Science Letters, v. 193, p. 483–499, doi:10.1016/S0012-821X(01)00481-2.

Pignotta, G.S., Paterson, S.R., Coyne, C.C., Anderson, J.L., and Onezime, J., 2010, Processes involved during incremental growth of the Jackass Lakes pluton, central Sierra Nevada batholith: Geosphere, v. 6, p. 130–159, doi:10.1130/GES00224.1.

Rapp, R.P., Watson, E.B., and Miller, C.F., 1991, Partial melting of amphibolites/eclogite and the origin of Archean trondhjemites and tonalites: Precambrian Research, v. 51, p. 1–25, doi:10.1016/0301-9268(91)90092-O.

Ratajeski, K., Glazner, A.F., and Miller, B.V., 2001, Geology and geochemistry of mafic to felsic plutonic rocks in the Cretaceous intrusive suite of Yosemite Valley, California: Geological Society of America Bulletin, v. 113, p. 1486–1502, doi:10.1130/0016-7606(2001)113<1486:GAGOMT>2.0.CO;2.

Ratajeski, K., Sisson, T.W., and Glazner, A.F., 2005, Experimental and geochemical evidence for derivation of the El Capitan Granite, California, by partial melting of hydrous gabbroic lower crust: Contributions to Mineralogy and Petrology, v. 149, p. 713–734, doi:10.1007/s00410-005-0677-4.

Reid, J.B., Evans, O.C., and Fates, D.G., 1983, Magma mixing in granitic rocks of the central Sierra Nevada, California: Earth and Planetary Science Letters, v. 66, p. 243–261, doi:10.1016/0012-821X(83)90139-5.

Reid, J.B., Murray, D.P., Hermes, O.D., and Steig, E.J., 1993, Fractional crystallization in granites of the Sierra Nevada: How important is it?: Geology, v. 21, p. 587–590, doi:10.1130/0091-7613(1993)021<0587:FCIGOT>2.3.CO;2.

Rollinson, H., 1993, Using geochemical data: Evaluation, presentation, interpretation: Singapore, Longman Singapore Publishers (Pte) Ltd., 352 p.

Ross, D.C., 1958, Igneous and metamorphic rocks of parts of Sequoia and Kings Canyon National Parks, California: California Department of Natural Resources, Division of Mines Special Report 53, 24 p.

Rudnick, R.L., and Fountain, D.M., 1995, Nature and composition of the continental crust: A lower crustal perspective: Reviews of Geophysics, v. 33, p. 267–309, doi:10.1029/95RG01302.

Rudnick, R.L., and Gao, S., 2003, The composition of the continental crust, *in* Rudnick, R.L., ed., The crust: Treatise on Geochemistry 3: Amsterdam, Elsevier, p. 1–64.

Rushmer, T., 1991, Partial melting of two amphibolites: Contrasting experimental results under fluid-absent conditions: Contributions to Mineralogy and Petrology, v. 107, p. 41–59, doi:10.1007/BF00311184.

Rushmer, T., 1996, Melt segregation in the lower crust: How have experiments helped us?: Royal Society of Edinburgh Transactions, Earth Sciences, v. 87, p. 73–83, doi:10.1017/S0263593300006490.

Saleeby, J., 2011, Geochemical mapping of the Kings-Kaweah ophiolite belt, California—Evidence for progressive mélange formation in a large offset transform-subduction initiation environment, *in* Wakabayashi, J., and Dilek, Y., eds., Mélanges: Processes of formation and societal significance: Geological Society of

America Special Paper 480, p. 31–73, doi:10.1130/2011.2480(02).

Saleeby, J.B., and Busby, C., 1993, Paleogeographic and tectonic setting of axial and western metamorphic framework rocks of the southern Sierra Nevada, California, *in* Dunne, G., and McDougall, K., eds., Mesozoic paleogeography of the western United States—II: Pacific Section, SEPM (Society for Sedimentary Geology) Book 71, p. 197–225.

Saleeby, J.B., Kistler, R.W., Longiaru, S., Moore, J.G., and Nokleberg, W.J., 1990, Middle Cretaceous silicic metavolcanic rocks in the Kings Canyon area, central Sierra Nevada, California, *in* Anderson, J.L., ed., The nature and origin of Cordilleran magmatism: Geological Society of America Memoir 174, p. 251–270.

Saleeby, J., Ducea, M., and Clemens-Knott, D., 2003, Production and loss of high-density batholithic root, southern Sierra Nevada, California: Tectonics, v. 22, p. 1064–1087, doi:10.1029/2002TC001374.

Saleeby, J., Ducea, M.N., Busby, C., Nadin, E., and Wetmore, P.H., 2008, Chronology of pluton emplacement and regional deformation in the southern Sierra Nevada batholith, California, *in* Wright, J.E., and Shervais, J.W., eds., Ophiolites, arcs, and batholiths: A tribute to Cliff Hopson: Geological Society of America Special Paper 438, p. 397–427, doi:10.1130/2008.2438(14).

Sawyer, E.W., 1994, Melt segregation in the continental crust: Geology, v. 22, p. 1019–1022, doi:10.1130/0091-7613(1994)022<1019:MSITCC>2.3.CO;2.

Shaw, D.M., 1970, Trace element fractionation during anatexis: Geochimica et Cosmochimica Acta, v. 34, p. 237–243, doi:10.1016/0016-7037(70)90009-8.

Sisson, T.W., and Moore, J.G., 1994, Geologic map of the Giant Forest Quadrangle, Tulare County, California: U.S. Geological Survey Geologic Quadrangle Map GQ-1751, scale 1:62,500.

Sisson, T.W., Grove, T.L., and Coleman, D.S., 1996, Hornblende gabbro sill complex at Onion Valley, California, and a mixing origin for the Sierra Nevada batholith: Contributions to Mineralogy and Petrology, v. 126, p. 81–108, doi:10.1007/s004100050237.

Sisson, T.W., Ratajeski, K., Hankins, W.G., and Glazner, A.F., 2005, Voluminous granitic magmas from common basaltic sources: Contributions to Mineralogy and Petrology, v. 148, p. 635–661, doi:10.1007/s00410-004-0632-9.

Skjerlie, K.P., and Johnston, A.D., 1993, Fluid-absent melting behavior of an F-rich tonalitic gneiss at mid-crustal pressures: Implications for the generation of anorogenic granite: Journal of Petrology, v. 34, p. 785–815, doi:10.1093/petrology/34.4.785.

Skjerlie, K.P., and Johnston, A.D., 1996, Vapour-absent melting from 10 to 20 kbar of crustal rocks that contain multiple hydrous phases: Implications for anatexis in the deep to very deep continental crust and active continental margins: Journal of Petrology, v. 37, p. 661–691, doi:10.1093/petrology/37.3.661.

Skjerlie, K.P., and Patiño-Douce, A.E., 2002, The fluid-absent partial melting of a zoisite-bearing quartz eclogite from 1.0 to 3.2 Gpa: Implications for melting in thickened continental crust and for subduction-zone processes: Journal of Petrology, v. 43, p. 291–314, doi:10.1093/petrology/43.2.291.

Spulber, S.D., and Rutherford, M.J., 1983, The origin of rhyolite and plagiogranite in oceanic crust: An experimental study: Journal of Petrology, v. 24, p. 1–25, doi:10.1093/petrology/24.1.1.

Stern, T.W., Bateman, P.C., Morgan, B.A., Newell, M.F., and Peck, D.L., 1981, Isotopic U-Pb ages of zircon from the granitoids of the central Sierra Nevada, California: U.S. Geological Survey Professional Paper 1185, 17 p.

Streckeisen, A., 1976, To each plutonic rock its proper name: Earth-Science Reviews, v. 12, p. 1–33, doi:10.1016/0012-8252(76)90052-0.

Wenner, J.M., and Coleman, D.S., 2004, Magma mixing and Cretaceous crustal growth: Geology and geochemistry of granites in the central Sierra Nevada batholith, California: International Geology Review, v. 46, p. 880–903, doi:10.2747/0020-6814.46.10.880.

Whitney, D.L., and Evans, B.W., 2010, Abbreviations for names of rock-forming minerals: American Mineralogist, v. 95, p. 185–187, doi:10.2138/am.2010.3371.

Williams, I.S., 1997, U-Th-Pb geochronology by ion microprobe: Not just ages but histories: Society of Economic Geologists Reviews in Economic Geology, v. 7, p. 1–35.

Wilson, M., 1989, Igneous Petrogenesis: London, Unwin Hyman, 466 p.

Wooden, J.L., Mazdab, F.K., and Barth, A.P., 2007, Hf and temperature (from Ti) variations in zircon: A potential new tool to evaluate petrologic processes in magmas: Geological Society of America Abstracts with Programs, v. 39, no. 6, p. 406.

Zeng, L., Ducea, M., and Saleeby, J.B., 2005, Geochemical characteristics of crustal anatexis during the formation of migmatite at the southern Sierra Nevada, California: Contributions to Mineralogy and Petrology, v. 150, p. 386–402, doi:10.1007/s00410-005-0010-2.